

AD-758 009

NUMERICAL STUDY OF PLUME-INDUCED FLOW
SEPARATION

L. Walitt, et al

Applied Theory, Incorporated

Prepared for:

Office of Naval Research
Advanced Research Projects Agency

March 1973

DISTRIBUTED BY:

NTIS

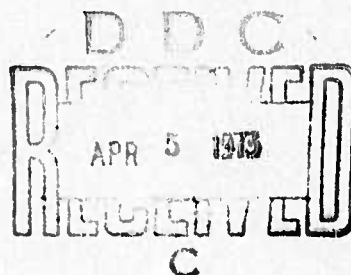
National Technical Information Service
U. S. DEPARTMENT OF COMMERCE
5285 Port Royal Road, Springfield Va. 22151

ATR-72-33-1

AD758009

SEMI-ANNUAL TECHNICAL REPORT
NUMERICAL STUDY OF PLUME-INDUCED FLOW SEPARATION

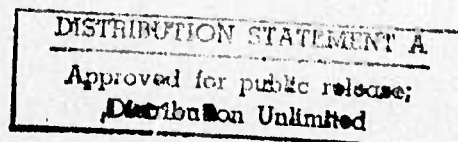
by
L. Walitt
D. C. Wilcox
C. Y. Liu



Details of illustrations in
this document may be better
studied on microfiche

March 1973

Reproduced by
NATIONAL TECHNICAL
INFORMATION SERVICE
U S Department of Commerce
Springfield VA 22151



1010 WESTWOOD BOULEVARD
LOS ANGELES, CALIFORNIA 90024
Telephone (213) 479-4379

Applied Theory, Inc.

R

SEMI-ANNUAL TECHNICAL REPORT

ATR-72-33-1

NUMERICAL STUDY OF PLUME-INDUCED FLOW SEPARATION

by

L. WALITT

D. C. WILCOX

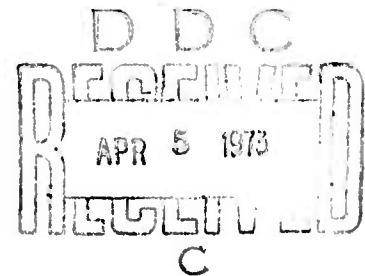
C. Y. LIU

The work reported herein was sponsored by the
Advanced Research Projects Agency
and was performed under Contract No. N00014-71-C-0331
ARPA Order No. 1801

for

Office of Naval Research
Department of the Navy
Arlington, Virginia

March 1973



APPLIED THEORY, INC.
1010 Westwood Boulevard
Los Angeles, California 90024

DISTRIBUTION STATEMENT A

Approved for public release;
Distribution Unlimited

The views and conclusions contained in this document are those of the authors and should not be interpreted as necessarily representing the official policies, either expressed or implied, of the Advanced Research Projects Agency or the U. S. Government.

ACKNOWLEDGEMENT

Dr. John G. Trulio of Applied Theory, Inc., gave invaluable guidance and assistance to this work. Professor Philip G. Saffman of the California Institute of Technology and Dr. Richard Lee of the Aerospace Corporation assisted in interpretation of the numerical data.

TABLE OF CONTENTS

SECTION		PAGE
	ABSTRACT	iii
1.	INTRODUCTION	1
2.	THE AFTON 2A COMPUTER CODE	3
3.	A CALCULATION OF SEPARATION-FREE PLUME FLOW	6
	3.1 Statement of the Problem	6
	3.2 Application of AFTON 2A	6
	3.3 Description of the Calculated Flow Field	10
4.	A CALCULATION OF PLUME-INDUCED FLOW SEPARATION	13
	4.1 Statement of the Problem	13
	4.2 Application of AFTON 2A	13
	4.3 Description of the Calculated Flow Field	15
5.	EVALUATION OF THE TWO COMPUTED FLOW FIELDS	19
	5.1 Boundary Layer Separation	19
	5.2 Inner Core Structure	21
	5.3 Axial Force	22
	5.4 Plume Scaling Laws	25
	5.5 Other Comparisons	26
6.	SUMMARY AND CONCLUSIONS	29
 APPENDIXES		
A	NUMERICAL TECHNIQUES AND CODE MODIFICATIONS	66
	A.1 Mass Addition Modification to AFTON 2A	66
	A.2 Inclusion of Plume Rarefaction Effects in AFTON 2A	67
	A.3 Artificial Viscosity	68

TABLE OF CONTENTS (continued)

APPENDIXES		PAGE
A	NUMERICAL TECHNIQUES AND CODE MODIFICATIONS (continued)	
	A.4 Serial Calculation of Heat Conduction and Continuum Motion	70
	A.5 Streamline Tracing and Shock-Wave Mapping	71
B	A SCHEME FOR CALCULATING POSITION OF POINTS IN FINITE DIFFERENCE MESHES	72
C	PREDICTION OF SHOCK STRUCTURE IN THE INTER- ACTION REGION BY THE METHOD OF CHARACTERISTICS	80
D	EFFECTS OF NOSE BLUNTNES ON THE CONE FLOW FIELD	84
E	STABILITY CRITERIA FOR AFTON 2A	87
	REFERENCES	

UNCLASSIFIED

Security Classification

DOCUMENT CONTROL DATA - R & D

(Security classification of title, body of abstract and indexing annotation must be entered when the overall report is classified)

1. ORIGINATING ACTIVITY (Corporate author) APPLIED THEORY, INC. 1010 Westwood Boulevard Los Angeles, California 90024		2a. REPORT SECURITY CLASSIFICATION UNCLASSIFIED	
		2b. GROUP	
3. REPORT TITLE NUMERICAL STUDY OF PLUME-INDUCED FLOW SEPARATION			
4. DESCRIPTIVE NOTES (Type of report and inclusive dates) Semi-Annual Technical Report			
5. AUTHOR(S) (First name, middle initial, last name) L. Walitt; D. C. Wilcox; C. Y. Liu			
6. REPORT DATE March 1973		7a. TOTAL NO. OF PAGES 99	7b. NO. OF REFS 30
8a. CONTRACT OR GRANT NO. N00014-71-C-0331		9a. ORIGINATOR'S REPORT NUMBER(S) ATR-72-33-1	
b. PROJECT NO.			
c.		9b. OTHER REPORT NO(S) (Any other numbers that may be assigned this report)	
d.			
10. DISTRIBUTION STATEMENT Approved for public release; distribution unlimited.			
11. SUPPLEMENTARY NOTES Details of illustrations in this document may be better studied on microfiche		12. SPONSORING MILITARY ACTIVITY Department of the Navy Office of Naval Research	
13. ABSTRACT <p>Laminar Mach 26 flow past a blunt-nosed cone with a spherical after-body that injects mass axially from its base into the air, was studied in two finite difference calculations. The mass injection rate for both calculations was 0.15 lb/sec, and Reynolds numbers relative to base diameter were 735 and 4130. Computations were performed with a code (AFTON 2A) which, apart from discretization error, generates solutions to the time-dependent Navier-Stokes equations for axisymmetric systems that contain mass-injecting bodies. In both cases steady flow was approached asymptotically in time from initial flow fields derived from simple inviscid theory.</p> <p>At the lower Reynolds number, the cone and after-body boundary layers remained attached, and the interaction between the incident airstream and the injected plume gases was similar to that of two impinging supersonic streams. By contrast, at the higher Reynolds number the cone and after-body boundary layers both separated, giving rise to a double-vortex pattern and a complex system of shock waves.</p> <p>AFTON 2A results were compared with a theoretical inviscid model of a mass source in a uniform hypersonic stream. In the AFTON 2A calculations, the predicted plume radius was much larger than that of the model, with an increased plume volume caused by heat transfer across the dividing streamlines. Although absolute magnitudes of plume-shock and dividing-streamline radii did not follow the inviscid scaling law, ratios of the radii were found to vary inversely as the fourth root of the plume drag coefficient, in accord with inviscid scaling.</p> <p>The two calculations also demonstrated a structural difference in the plume inner core. At the lower Reynolds number the inner core was nearly isentropic, whereas at the higher Reynolds number heat penetrated the plume core in an amount sufficient to produce significant entropy gradients.</p>			

DD FORM 1 NOV 65 1473

19

UNCLASSIFIED

Security Classification

ABSTRACT

Laminar Mach 26 flow past a blunt-nosed cone with a spherical after-body that injects mass axially from its base into the air, was studied in two finite difference calculations. The mass injection rate for both calculations was 0.15 lb/sec, and Reynolds numbers relative to base diameter were 735 and 4150. Computations were performed with a code (AFTON 2A) which, apart from discretization error, generates solutions to the time-dependent Navier-Stokes equations for axisymmetric systems that contain mass-injecting bodies. In both cases steady flow was approached asymptotically in time from initial flow fields derived from simple inviscid theory.

At the lower Reynolds number, the cone and after-body boundary layers remained attached, and the interaction between the incident airstream and the injected plume gases was similar to that of two impinging supersonic streams. By contrast, at the higher Reynolds number the cone and after-body boundary layers both separated, giving rise to a double-vortex pattern and a complex system of shock waves.

AFTON 2A results were compared with a theoretical inviscid model of a mass source in a uniform hypersonic stream. In the AFTON 2A calculations, the predicted plume radius was much larger than that of the model, with an increased plume volume caused by heat transfer across the dividing streamline. Although absolute magnitudes of plume-shock and dividing-streamline radii did not follow the inviscid scaling law, ratios of the radii were found to vary inversely as the fourth root of the plume drag coefficient, in accord with inviscid scaling.

The two calculations also demonstrated a structural difference in the plume inner core. At the lower Reynolds number the inner core was nearly isentropic, whereas at the higher Reynolds number heat penetrated the plume core in an amount sufficient to produce significant entropy gradients.

1. INTRODUCTION

Two low-Reynolds-number calculations were made of complete hypersonic plume-body flow fields governed by the Navier-Stokes equations. Results of the calculations, and the computational procedures employed, are reported herein.

Interest in the interaction of a jet plume with a hypersonic free stream has attended the development of high-altitude rockets and re-entry vehicles. The importance of the near-body flow field then manifests itself in several ways: for example, exhaust plumes can induce flow separation on the surface of an aerodynamic object, creating conditions that interfere with the operation of sensing devices. However, plume-body interaction has generally been ignored in past analytical studies of plume-hypersonic-airstream interaction, with attention focused instead upon far-field behavior.¹⁻⁵ Further, while heat conduction effects have been included in some prior calculations of plume flow, heat transfer has always been assumed negligible below the inner shock; the plume inner core is then approximated as isentropic. Only one pertinent near-field study appears to have been performed, and that in support of an experimental investigation of plume-body-airstream interaction;⁶ guided by observed flow field structure, an analytical model was developed to predict separation on a cone and other near-cone flow phenomena. Each of the referenced investigations¹⁻⁶ has been carried out by methods specialized with respect to both flow conditions and body geometry.

Some experiments have been conducted to study base injection, but generally at Reynolds numbers much higher than those encountered under high-altitude flight conditions. Of

special relevance is the work of Boger, Rosenbaum and Reeves⁶, which included wind-tunnel measurements for Mach 10 flow past a 6-degree-half-angle, flat-based cone with axial base injection; the Reynolds number range covered was $1.3 \cdot 10^5$ to $1.3 \cdot 10^6$.[†] A Reynolds number of a few thousand is not uncommon for hypersonic re-entry vehicles at altitudes above 100 km. Such low Reynolds numbers are difficult, if not impossible, to produce in a wind tunnel at hypersonic speeds; on the other hand, for full-scale vehicles under real flight conditions, instrumentation is insufficient to determine any but gross flow properties, thus emphasizing the need for more precise theoretical methods.

The two flow fields considered here were calculated in finite difference approximation using a computer code called AFTON 2A. The AFTON 2A code is based on finite difference equations for unsteady axisymmetric continuum motion; underlying the equations is a general method for writing discrete analogs of the laws governing classical fields. For both calculations the body was a blunt-nosed cone with a spherical after-body, the free-stream Mach number was 26, and the mass injection rate was 0.15 lb/sec. Reynolds numbers for the two cases were 735 and 4150 - flow conditions that correspond to a free-stream velocity of 22,500 fps and altitudes of 300,000 and 270,000 feet, respectively.

In Section 2 below the AFTON 2A computer code is described; calculations for the two different Reynolds numbers are discussed in Sections 3 and 4, while in Section 5 the two flow fields are compared; Section 6 contains a summary of the results of the program and associated conclusions.

[†] Unless otherwise stated, all Reynolds numbers herein are based on free-stream flow conditions, and on the maximum length subtended by the body normal to the free-stream flow direction.

2. THE AFTON 2A COMPUTER CODE

For the present program, the AFTON 2A computer code was used to integrate the Navier-Stokes equations for time-dependent compressible axisymmetric flow with mass injection. AFTON 2A is one of a set of computer codes known as the "AFTON" codes. Many laminar flow fields have been computed with the AFTON codes, and the accuracy of numerical flow fields so generated has been evaluated. Among the motions calculated have been aerodynamic flow around objects of practical interest under conditions of two-dimensional plane⁷⁻¹² and axial¹³ symmetry, and for fully asymmetric three-dimensional¹⁴ systems. In most cases, as in the present study, first-of-a-kind numerical solutions have been developed to the complete flow equations, including the effects of compressibility, heat conduction, viscosity, and mass addition.

A generalized form of the discrete equations of von Neumann and Richtmyer¹⁵ comprises the basis for the AFTON codes. The generalized equations, which have been used successfully not only in solving gasdynamic problems but in many other branches of continuum mechanics as well, are of the "time-marching" kind; time is used as an independent mechanical variable and the solution of any given problem of motion proceeds through a series of stepwise advances in time. Similarly the space continuum is replaced for numerical purposes by a discrete set of points termed a "finite difference mesh"; alternatively, the points of a finite difference mesh can be considered as the vertices of polyhedra of finite size, termed "cells" or "zones", that subdivide physical space in one-to-one fashion. At each timestep the dependent variables of the motion are

updated in each cell of a given finite difference mesh, in accord with discrete analogs of the equations of continuum motion.

The principle used to deduce the AFTON finite difference equations is applicable to all the fields of classical physics, and insures that certain fundamental transformation properties of classical continua are preserved exactly in the finite difference equations that issue from it; moreover, the finite difference equations so obtained are unique in preserving those transformation properties. Specifically, for example, the AFTON finite difference analogs of the equations for mass conservation, momentum conservation, and the First Law of thermodynamics, can be shown by rigorous algebraic manipulation to imply exact conservation of total energy in each zone, or all, of a finite difference mesh, just as in the case of the corresponding differential equations of motion of a continuous medium. The success of the AFTON difference equations is thought to be due, at least in part, to their energy conservation properties. A more detailed discussion of the transformation properties of the AFTON equations is given in References 16 through 19.

A modest amount of code modification was required to make AFTON 2A suitable for plume-body interaction calculations; the code was altered in four ways:

- (1) Provision was made for axial mass addition from the base of the body;
- (2) Changes were made to insure that plume rarefaction effects would be accurately accounted for;

- (3) An artificial viscous stress, differing from zero only in the near-vicinity to the shock front that encloses the total region of disturbed flow, was incorporated into the code;
- (4) A procedure was developed for the serial calculation of heat conduction and hydrodynamic motion, and included in the computational scheme.

The four modifications are discussed in Appendix A.

3. A CALCULATION OF SEPARATION-FREE PLUME FLOW

The first of two AFTON-calculated hypersonic-airstream-plume-interaction flow fields is described below. Computational details are presented in Section 3.2. Results of the calculation are given in Section 3.3, including comparisons with the predictions of an inviscid theory.

3.1 STATEMENT OF THE PROBLEM

The problem addressed is that of calculating the field of steady flow past a conical body (Figure 1), with particular emphasis on the features of the near field. Nondissociated air, whose properties are defined in Table 1, flows past the conical body at Mach 26; the Reynolds number for the flow is 735. The body is at zero angle-of-attack and ejects air at a rate of 0.15 lb/sec, corresponding to a ratio of plenum-chamber pressure to ambient pressure (p_c/p_∞) of $5.76 \cdot 10^6$. Since boundary-layer separation does not occur, the calculation is referred to subsequently as the separation-free plume calculation.

3.2 APPLICATION OF AFTON 2A

The finite difference mesh used in the separation-free plume calculation (Figure 2) was generated by a technique developed for the present study (Appendix B). The mesh consists of the intersection of 35 streamline-like lines with 224 potential-like lines. Zones are closely spaced in the vicinity of the body (including two zones to define the sonic orifice) and gradually increase in size with distance from the body.

Table 1. Assumed Thermodynamic Properties of Nondissociated Air

PROPERTY	DESCRIPTION OF ASSUMED VARIATION	EQUATION
State Equation	Perfect gas with constant specific heat ratio, $\gamma = 1.4$	$p = (\gamma - 1) \rho E$
Prandtl Number	Constant	$P_r = 0.72$
Molecular Viscosity	Approximation to the low temperature data of Batt and Kubota ²⁰ for temperature below 450° R; approximation to the Sutherland law above 450° R. Reference conditions are $\mu_r = 7.0577 \cdot 10^{-8}$ lb-sec/ft ² and $T_r = 86^\circ$ R.	$\frac{\mu}{\mu_r} = \begin{cases} \left(\frac{T}{T_r}\right)^{0.9875}, & \frac{T}{T_r} \leq 3.2 \\ 1.205 \left(\frac{T}{T_r}\right)^{0.862}, & 3.2 < \frac{T}{T_r} \leq 5.2 \\ 1.310 \left(\frac{T}{T_r}\right)^{0.786}, & 5.2 < \frac{T}{T_r} \leq 10 \\ 1.545 \left(\frac{T}{T_r}\right)^{0.569}, & \frac{T}{T_r} > 10 \end{cases}$

Density, specific internal energy and fluid velocity assumed their free-stream values at the upstream boundary of the mesh. A no-slip velocity boundary condition was enforced at the surface of the cone, which was assumed isothermal at a temperature of 540°R. Frictionless flow was maintained along the axis and along the top of the mesh (or lateral boundary); particle velocities at mesh points along the system's axis were updated by the same equations used at interior points, but taking into account the symmetry of the field about that axis. Boundary conditions based on the method of characteristics for inviscid flow^{9,12,13} were employed at the downstream boundary. Conditions at the sonic orifice were characterized by the following values of injection density, ρ^* , specific internal energy, E^* , and velocity, U^* :

$$\left. \begin{aligned} \frac{\rho^*}{\rho_{t_\infty}} &= 0.7050 \\ \frac{E^*}{E_{t_\infty}} &= 0.1675 \\ \frac{U^*}{U_\infty} &= 0.1535 \end{aligned} \right\} \quad (1)$$

In Equation (1), ρ_{t_∞} and E_{t_∞} are the free-stream stagnation density and specific internal energy, respectively; U_∞ is the free-stream velocity.

Initial conditions for the calculation were based primarily on inviscid theories. For example, flow near the nose of the cone was determined from Newtonian Theory, while elsewhere near the cone surface approximate flow

conditions were obtained by recourse to conical shock-wave theory. Also, plume properties were defined from the "universal" correlation (developed by Jarvinen and Hill¹) of solutions obtained by the method of characteristics. Viscous effects were accounted for near the cone surface where the merged viscous-shock layer was approximated with linear velocity profiles. A velocity vector plot of the initial flow field is presented in Figure 3, in which the vectors emanate from mesh points and have magnitudes proportional to local flow speed.

As noted in Section 2 and Appendix A, an artificial viscosity was used only in the near-vicinity of the shock surface that formed an inner boundary of the region of free-stream flow. As part of a numerical experiment, a portion of the calculation was repeated using the artificial viscosity in the plume-body interaction region as well; the resulting changes in the computed flow field were negligible.

The calculation was carried out in the following three steps: first with the full mesh shown in Figure 2, then on the portion of the mesh downstream of Curve 1, and finally on the portion of the mesh downstream of dashed Curve 2. The equations of motion were integrated in the first part of the calculation to a characteristic time, τ , of 1.12 (unit characteristic time corresponds to the time required for a free-stream fluid particle to travel one base diameter). Fluid property variations with time were examined throughout the mesh. It was found that upstream of the dashed Curve 1 of Figure 2 the flow was not changing appreciably with time when τ reached the value 1.12; as an example, the time-variation of pressure along the cone surface is shown in

Figure 4. Hence, there was no point in continuing to update the flow field upstream of Curve 1. The second part of the computation was therefore confined to the region downstream of Curve 1 which became the upstream boundary of a truncated mesh. Flow-field variables along the boundary did not change with time during the second step of the computation, which required an additional 0.49 units of characteristic time. In the third step, the upstream boundary was moved to Curve 2 of Figure 2, and an additional 0.14 units of characteristic time was required for the flow variables in the reduced mesh to asymptote to "infinite" time values. Again, attainment of steady flow was established by investigating the temporal variation of flow properties throughout the flow field (e.g., see Figures 4 through 7). The separation-free plume calculation was carried out to a characteristic time of 1.75; required computing time was equivalent to 3.4 hours on a CDC 7600 computer.

3.3 DESCRIPTION OF THE CALCULATED FLOW FIELD

A velocity vector plot of the numerical flow field in the vicinity of the base of the body is shown in Figure 8. No boundary-layer separation appears, and the resulting flow field resembles the collision of two supersonic streams.

In Figure 8, heavy solid lines denote three shock waves in the interaction region. The thin solid line traces the streamline separating the free stream and the plume gases. (The methods employed to trace the dividing streamline and map the shock waves are described in Appendix A.) Two shocks lie in the airstream with a third in the plume gases. The airstream shocks are the conventional cone shock and plume shock. The cone shock is caused by the vehicle geometry which turns the free-stream flow. The plume shock is present to turn the

airstream about the effective plume body defined by the dividing streamline. The shock in the plume gases, which is referred to as the inner shock, likewise turns the plume flow to accommodate the effective body shape presented by the dividing streamline.

The importance of viscous and thermal diffusion effects becomes apparent when the separation-free calculation is compared to inviscid predictions. The most complete inviscid description of a hypersonic-stream-plume-interaction flow field is provided by the Jarvinen-Hill model¹ of a mass source in a uniform hypersonic stream. Calculated shocks and dividing streamline are compared to Jarvinen-Hill predictions in Figure 9. Predicted inner-shock positions differ little; however, plume-shock and dividing streamline radii are predicted to be much larger by the AFTON 2A calculation than by the Jarvinen-Hill theory. Specifically, the dividing streamline radius for the numerical flow field is approximately 60 percent larger than the inviscid result at distances greater than one and one-half base diameters downstream of the base.

An explanation for the increased plume volume can be perceived in the calculated internal energy contours shown in Figure 10. Strong temperature gradients exist in the vicinity of and normal to the dividing streamline; hence, substantial heat transfer across the plume boundary causes hotter plume gases than in inviscid predictions, with an attendant increase in plume volume.

Although some current plume models account for viscous and heat-conduction effects, all assume that an inviscid, isentropic core exists below the inner shock. Since inner core conditions

have a pronounced effect on the Mach disc, the inner core can conceivably affect the flow field far beyond the near-body region; the isentropic-inner-core hypothesis was therefore examined. Calculated pressure (p), density (ρ), and Mach number (M) contours are shown in Figures 11, 12 and 13, respectively. Contours below the inner shock indicate that the flow is source-like in the inner core (i.e., constant-density surfaces are approximately spheres centered at the injection orifice), which is the structure postulated in the Jarvinen-Hill theory. The three sets of contours are similar; hence, all three flow properties can be expressed as a function of any one of the three, just as in isentropic flow. Figure 14 indicates the variation of p as a function of ρ along both the system axis and two streamlines in the inner core; the streamline locations are shown in Figure 13. Figure 14, a log-log plot, presents an almost straight line whose slope is 1.375, very close to the assumed specific heat ratio of air ($\gamma = 1.4$); p/ρ^γ is therefore nearly constant along streamlines in the inner core, and the flow there is approximately isentropic.

In summary, three significant features of the plume-body flow field have been noted; flow separation does not occur for the assumed flow conditions, which include a Reynolds number of 735; heat transfer across the dividing streamline increases the plume volume over the size predicted by inviscid theories; the region below the inner shock is isentropic. The separation-free plume predictions are compared further with other theories and experimental data in Section 5, but before that the second of the two calculations is described (Section 4).

4. A CALCULATION OF PLUME-INDUCED FLOW SEPARATION

4.1 STATEMENT OF THE PROBLEM

As with the separation-free plume calculation described in Section 3, Mach 26 air flow passes over the body shown in Figure 1; however, the Reynolds number is increased to 4150. The body is again at zero angle-of-attack and emits 0.15 lb/sec of air, corresponding to a reduced ratio of plenum-chamber pressure to ambient pressure of $1.04 \cdot 10^6$. In contrast to the computation discussed in Section 3, the cone and afterbody boundary layers separate at the increased Reynolds number. The calculation is therefore referred to as the separation-plume calculation.

4.2 APPLICATION OF AFTON 2A

The separation-plume calculation was performed in three distinct steps. In the first step the full finite difference mesh used for the separation-free plume calculation was employed (Figure 2); it was expected that the higher-Reynolds-number flow field would be so similar to that at the lower Reynolds number that the same mesh would suffice to define flow details for both. The steady flow field variables of the separation-free plume calculation were used as initial data, except that (a) the density, ρ , above the dividing streamline was increased by a factor of 5.6 in order to achieve a Reynolds number of 4150 and (b) the specific internal energy above the inner shock was decreased by one percent to provide the temperature appropriate to an altitude of 270,000 ft. Steady flow conditions were reached at a calculated characteristic time of 6.58 (Figure 15).

In the second step the density of mesh points was greatly increased in the near-body region to obtain better definition of base flow details. To that end, twenty streamline-like lines were added to the original finite difference mesh, yielding the mesh shown in Figure 16. Initial conditions for the calculation of step two were obtained by linear interpolation in the flow field obtained from the first calculational step. A modest amount of flow-field adjustment occurred in a few cycles and smaller changes took place thereafter. In close analogy with the separation-free plume calculation, the flow field was soon found steady upstream of the dashed line of Figure 16, in this case after advancing the solution in time by .07 characteristic units. Values of the flow field variables along the dashed line therefore provided accurate upstream flow conditions for the third calculational step, in which computation was confined to that portion of the mesh of Figure 16 downstream of the dashed line. The equations of motion were integrated over the reduced mesh for another 1.5 units of characteristic time, when steady flow was achieved (Figures 17, 18 and 19).

In all three steps the boundary conditions were identical to those employed in the separation-free plume calculation. The artificial viscosity was again localized to the cone and plume shocks above the interaction region, with a single exception noted below.

Overall, the separation-plume calculation was carried to a characteristic time of 8.15 on a UNIVAC 1108 computer, and required the equivalent of 9.8 hours on a CDC 7600 computer

for its completion. Three factors caused an increase in computing time (relative to the nonseparated case). First, scaling the low-Reynolds-number flow field yielded an initial field with much more internal energy than was appropriate to the higher Reynolds number; converging to the less dissipative high-Reynolds-number flow field was a time-consuming process. Secondly, the artificial viscosity was used at the outset in the interaction region; however, as the calculation proceeded, the artificial viscosity assumed non-zero values outside shock layers and therefore had to be removed. To avoid numerical difficulties, it was necessary to eliminate the artificial viscosity gradually, over a substantial number of calculational cycles. Finally, the computed flow field was far more complicated than the separation-free field described in Section 3, and therefore took longer to compute; the higher-Reynolds-number field contained a region of separation and a complicated system of shocks in the interaction region.

4.3 DESCRIPTION OF THE CALCULATED FLOW FIELD

The flow field at a Reynolds number of 4150 is quite unlike that observed in the separation-free plume calculation of Section 3. The cone and after-body boundary layers both separate, giving rise to a double vortex pattern (referred to as the separation bubble) and a complex system of shock waves. Figure 20 shows the flow field near the base, including the system of predicted shocks. There are five shock waves in the interaction region, including three in the airstream and two in the plume gases. The airstream shocks are the cone

shock, the airstream separation shock, and the plume shock. The airstream separation shock is required to turn the flow at the upstream edge of the separation bubble. Only one of the plume-gas shocks is shown in Figure 20, namely, the plume separation shock (also caused by the separation bubble) which turns very rapidly at the point of contact of (a) air flowing around the upstream portion of the separation bubble, and (b) plume gases flowing over the bubble's downstream side. The other plume-gas shock, or "inner" shock, is first seen approximately one base diameter downstream of the base; delayed formation of the inner shock will be discussed further below.

Qualitative structure of the higher-Reynolds-number flow field is similar to that recorded⁶ in a shadowgraph taken of the flow past a 12-degree flat-based cone at Mach 10 and Reynolds number $1.34 \cdot 10^5$. That the shadowgraph (Figure 21) exhibits the same complicated multiple-shock system as that calculated here was established independently by Boger, Rosenbaum and Reeves⁶ in a careful, exhaustive analysis; since their work is not easily accessible, a more complete account of the shadowgraph analysis is presented in Appendix C.

As in the lower-Reynolds-number flow field, the plume shock and dividing streamline radii are predicted by the AFTON 2A calculation to be much larger than their inviscid counterparts. The near-field structure is compared to the Jarvinen-Hill predictions in Figure 22. Beyond 1.5 base-diameters downstream of the injection orifice, the fractional increase of 55% in plume size is slightly less than the fractional increase found at the lower Reynolds number (60%). A smaller fractional increase in plume size is consistent with a reduction, relative to the

flow at lower Reynolds number, in the amount of heat conduction across the dividing streamline; such reduction might be caused by the smaller thermal diffusivity associated with the higher Reynolds number. Verification of the hypothesis of reduced heat transfer across the plume boundary is obtained by comparing specific internal energy contours for the separated flow field (Figure 23) with specific internal energy contours for the case of low-Reynolds-number (Figure 10). Contours are more closely spaced and temperatures higher near the plume shock at Reynolds number 735 than in the separated case, indicating a higher heat transfer rate.

Unlike the separation-free plume calculation, there is an appreciable difference between the inner shock location predicted by AFTON 2A and that of Jarvinen and Hill. The AFTON 2A inner shock is about 25% further from the symmetry axis than its inviscid counterpart. Furthermore, inspection of Figures 24, 25 and 26 shows that the Mach number contours differ greatly from the pressure and density contours. Both types of observation suggest that the plume's inner core is not isentropic at the higher Reynolds number. Confirmation is provided by log-log plots of p versus ρ (Figure 27); the curves show the p - ρ relationship along the system axis and along two inner-core streamlines; the streamline locations are indicated in Figure 26. The slopes of the various curves lie between 1.30 and 1.33, indicating that p/ρ^Y , and hence the entropy, varies both across and along streamlines. Reasons for the enlarged nonisentropic inner core found in the separation-plume calculation are discussed in Section 5.

The inner shock does not appear upstream of the axial station $x/D = 1$ (Figure 22), which is also the approximate

end point of the plume separation shock. Appeal to Mach line behavior in the interaction region (Figure 28) provides an explanation of the mechanisms underlying midstream termination of the plume separation shock and delayed inner shock formation. The Mach lines shown in the figure are part of an expansion fan which emanates from the injection-orifice lip. The expansion fan catches and weakens the plume separation shock, whose strength is so reduced thereby that the shock is nearly parallel to a Mach line at $x/D = 1$. The expansion fan then reflects from the plume-separation shock as a compression wave which eventually becomes the inner shock. Steepening of the compression wave is evidenced by Mach line coalescence after reflection.

Summarizing, four significant points have been noted regarding the separation-plume calculation: the cone and after-body boundary layers separate at the increased Reynolds number of 4150; heat transfer across the dividing streamline causes approximately the same fractional plume volume increase over inviscid prediction as the lower-Reynolds-number volume increase; the plume inner core is not isentropic; inner shock formation is delayed by interaction of the plume-separation shock with the expansion fan from the lip of the injection orifice.

5. EVALUATION OF THE TWO COMPUTED FLOW FIELDS

The separation-free plume flow field and the separated plume field differ markedly in boundary-layer separation and in inner-core structure. As will be discussed in the following sections, axial forces acting on the body are similar for the two plume flows and, surprisingly, the two calculated fields are consistent in one important respect with a simple scaling law. The streamline plots of Figure 29 show the main contrasts. Heavy solid lines denote the various shock waves present in the flow fields and the dashed lines define the dividing streamlines. The separation bubble of the higher-Reynolds-number flow occupies a region near the after-body within which lie two families of closed streamlines; each family outlines a region of recirculating vortical flow.

5.1 BOUNDARY LAYER SEPARATION

Boundary layer separation is observed for only one of the flow fields as is consistent with the Reynolds number difference; with decreasing Reynolds number, boundary layers become more stable and less likely to separate in an adverse pressure gradient.^{21,22} A criterion for stability of a boundary layer with respect to separation is often expressed in terms of a parameter which provides a measure of the relative importance of (a) the strength of the local pressure gradient and (b) the magnitude of the viscous stress. In particular the separation of classical boundary layers has been found empirically to take place in accord with the criterion $\Lambda \leq -12$ where Λ , the Pohlhausen parameter,²¹ is defined by the relation

$$\Lambda = - \frac{\rho_e}{\rho_w} \frac{\delta^2}{\mu_e U_e} \frac{dp}{ds} \quad (2)$$

In Equation (2) ρ_e , μ_e , U_e denote density, viscosity and velocity at the edge of the boundary layer, ρ_w is the fluid density at the solid boundary, δ is the boundary layer thickness and dp/ds is the streamwise pressure gradient.

The parameter Λ was evaluated for the calculated separation-plume and separation-free plume flows. Since both fields had merged viscous and shock layers, the boundary layer thickness was taken as the distance between the cone shock and the cone surface at the intersection of the cone and after-body; ρ_e , μ_e and U_e were assigned the free-stream values of density, viscosity and flow speed, respectively. The calculated pressure field was used to evaluate the gradient of pressure at a number of boundary-layer points near the base of the body, and dp/ds (Equation (2)) was equated to the maximum adverse gradient so computed. The wall density ρ_w was determined from the fluid's thermal equation of state using the known wall temperature and the surface pressure at the point of maximum adverse pressure gradient. It was found that Λ had the value -6.85 for the separation-free plume calculation and -16.0 for the separation-plume calculation, a result consistent with the Pohlhausen prediction that separation occurs for $\Lambda \leq -12$. Conformity with the Pohlhausen criterion is noteworthy whether it be interpreted as a further point of agreement of the calculations with basic flow field behavior, or as an indication that the criterion applies not only to classical boundary layers but also to boundary layers that merge with shocks.

5.2 INNER CORE STRUCTURE

Another major structural difference between the two computed flow fields occurs in the plume's inner core. As noted in earlier sections, the inner core is nearly isentropic for a Reynolds number of 735, whereas entropy varies in the core when the number is increased to 4150. Close examination of the flow field below the inner shock has made intelligible the relation between the computed cores.

Differences between the two inner cores are evident in the dissimilar Mach-number contour plots of Figures 13 and 26, whereas the streamline plots of Figure 29 indicate that the flow is source-like below the inner shock for both Reynolds numbers. Thus, it is reasonable to expect the dissimilar Mach-number fields to be associated with correspondingly different inner-core temperature fields. Inspection of specific internal energy (or, equivalently, temperature) contours in the inner-core region (Figures 30 and 31) shows that, to a distance of about three-quarters of a base diameter downstream of the orifice, the two flows are virtually identical; further downstream, however, the contours differ markedly. The inner-core temperature decays more rapidly with downstream distance at the lower Reynolds number, and the inner core is hotter when the Reynolds number is 4150 — results consistent with the observation in Section 4.3 that the fractional increase in inner-shock radius over inviscid predictions is noticeable only for the higher-Reynolds-number calculation.

Inner-core heating at Reynolds number 4150 is evidently a heat conduction effect; the closely-bunched specific internal energy contours near the inner shock indicate that strong

temperature gradients occur much closer to the axis at the higher Reynolds number than in the nonseparated case. Further, at a Reynolds number of 4150 the temperature near the inner shock is much higher than in the lower-Reynolds-number field (see Figures 30 and 31). The higher temperatures are a direct result of two sources of heat peculiar to the separated flow field, namely, intense shock heating in the interaction region from (a) the airstream separation shock and (b) the nearly normal plume shock. Heat generated in the interaction region is convected along streamlines, and penetrates the plume inner core by thermal conduction across streamlines.

A final point regarding the structure of the inner core can be noted from Figure 31. At the higher Reynolds number a large temperature gradient is present normal to the axis of the system and below the inner shock, in a region where streamlines are not parallel to isotherms. Heat therefore diffuses along streamlines of the higher-Reynolds-number field, causing some redistribution of energy within the inner core. Further study will be required in order to assess the effects of such heating on important plume features like the Mach disc.

5.3 AXIAL FORCE

It was found for both Reynolds numbers that rocket thrust far exceeded all other calculated axial forces on the body. Moreover, pressure and viscous forces caused the thrust to increase further, rather than to decrease; as can be seen from Table 2, the force increments were 9% and 4%, respectively, for Reynolds numbers 735 and 4150. In order to exhibit the magnitudes of the various forces acting, several axial force coefficients are presented in Table 2, namely, C_{x_R} , ΔC_x ,

Table 2. Axial Force Coefficients for the Re-entry Body at Two Altitudes.
Appropriate Reynolds numbers and rocket-chamber-to-ambient pressure ratios are shown.

Reynolds Number $Re_{\infty D}$	$\frac{P_c}{P_{\infty}}$	Axial Force Coefficient Due to Rocket Thrust C_{x_R}	Increment in Axial Force Coefficient Due to Pres- sure Forces ΔC_{x_p}	Increment in Axial Force Coefficient Due to Shear Forces ΔC_{x_r}	Total Increment in Axial Force Coefficient ΔC_{x_t}	Coefficient of Total Axial Force C_x
735	5.759×10^6	10.5209	.3773	.5616	.9389	11.4598
4150	1.041×10^6	1.8800	.0639	.0090	.0779	1.9579

ΔC_{x_p} , ΔC_{x_T} and C_x . The coefficient C_{x_R} is proportional to the axial force on the body due to the rocket thrust; specifically,

$$C_{x_R} = \frac{p^* A^* (1 + \gamma M^{*2})}{\frac{\pi}{4} D^2 q_\infty} \quad (3)$$

where A^* , p^* and M^* denote nozzle exit area, pressure and Mach number, respectively, and q_∞ is the free-stream dynamic pressure ($q_\infty = \frac{1}{2} \rho_\infty U_\infty^2$); the coefficients ΔC_x , ΔC_{x_p} , ΔC_{x_T} and C_x are similarly defined as the total axial aerodynamic force on the body, the axial pressure force on the body, the axial viscous force on the body and the total force on the body from all sources, respectively, divided in each case by the reference force $(\pi/4) D^2 q_\infty$. The axial components of the total aerodynamic force (ΔC_x) and the pressure force (ΔC_{x_p}), respectively, were computed by contracting the total stress and the stress due to pressure with a unit normal to the body surface, and integrating the axial component of the resulting product over the surface of the body (excluding the nozzle exit). ΔC_{x_T} was then calculated as the difference between ΔC_x and ΔC_{x_p} ; also, C_x was computed as the sum of C_{x_R} and ΔC_x .

A comparison of the axial-force coefficients of Table 2 with corresponding coefficients for the flat-based cone studied by Boger, Rosenbaum and Reeves⁶ indicates a definite advantage for the round-based configuration: The thrust is enhanced by the body even when boundary layer separation occurs. The explanation for the augmented thrust lies in the fact that rounding the base permits boundary layer separation to occur further downstream than in the case of a flat base. For a flat-based vehicle, the plume induces the separation region

to move forward from the flat base to the cone forebody with an attendant increase in drag (a decrease in thrust).

5.4 PLUME SCALING LAWS

Although the absolute magnitudes of calculated plume shock and dividing streamline radii differ from inviscid predictions, a surprising correspondence with the Jarvinen-Hill theory has been established: Calculated ratios of plume shock and dividing streamline radii obey the Jarvinen-Hill scaling laws. The correspondence is evident from the nearly identical fractional increases (over inviscid prediction) in plume size noted for the two calculations. For example, the stated scaling law for plume shock radius, r_p , is

$$r_p^2 = 0.726 \cdot x \cdot (\bar{D}/q_\infty)^{\frac{1}{2}} \quad (4)$$

where x is axial distance downstream of the mass source and \bar{D} is plume drag. The two calculated flow fields had the same plume drag and free-stream velocity; hence, at a fixed value of x , the plume shock radii are predicted by Equation (4) to vary as

$$\frac{r_p^{(735)}}{r_p^{(4150)}} = \left[\frac{\rho_\infty^{(4150)}}{\rho_\infty^{(735)}} \right]^{\frac{1}{4}} \quad (5)$$

where numerical superscripts are used to denote the Reynolds numbers at which the variable was calculated. Equation (5) is satisfied by the numerical data of the AFTON 2A calculations to within 7% at all points downstream of $x/D = 1.5$. The dividing streamline radius can similarly be shown for inviscid flow to vary inversely as the fourth root of free-stream density, and

ratios of the calculated dividing streamline radii again agree with the Jarvinen-Hill prediction to within 7%.

5.5 OTHER COMPARISONS

For both Reynolds numbers, some further quantitative comparisons of the numerical results have been made with the small set of pertinent theoretical and experimental data presently available. For example, the calculated bow shock strength at the centerline of the system lies within 5% of the theoretical value for both Reynolds numbers. For the calculation at a Reynolds number of 735 the density distribution differs by no more than 5% from the Jarvinen-Hill distribution along the system's centerline downstream of the injection orifice. Also, the computed cone shock angles were 9.8 and 10.0 degrees for Reynolds numbers 735 and 4150 respectively; the corresponding inviscid angle is 9.5 degrees.

In a final quantitative comparison presented in Figure 32, it can be seen that AFTON-2A-computed cone-surface pressures exhibit the same kind of variation with Reynolds number (based on position) as that found both experimentally and in previous theoretical predictions. AFTON 2A cone-surface-pressure distributions for both calculations appear in the figure together with cone-surface pressure data^{23,24} for a variety of cone flows. Pressure is given in units of Newtonian pressure and is shown as a function of a parameter, \tilde{x} , defined by the relation

$$\tilde{x} = \frac{M_{\infty}}{\sin^2 \theta_c} \sqrt{C^*/Re_{x_{\infty}}} \quad (6)$$

where θ_c is the cone half-angle and C^* is a constant of proportionality between temperature and viscosity. Nose-bluntness

effects²⁵ were found to be unimportant aft of a point halfway down the cone (Appendix D), and the numerical data are therefore presented for points downstream of the halfway point and upstream of the spherical base. Theoretical weak-interaction predictions of Probstein²⁶ and the strong-interaction prediction of Stewartson²⁷ are represented in the figure, along with the predicted free molecular limit for each cone flow.

Figure 32 indicates that surface pressures (● symbols) from the two calculations reported herein fall between the limits represented by hypersonic weak-interaction theory and free molecular flow. The trend followed by the computed pressures is consistent with Waldron's data for a 20-degree-half-angle cone (◊ symbols) which follow the Probstein weak-interaction prediction up to a value of $\tilde{\chi} \approx 2$ and then tend asymptotically toward the free molecular limit as $\tilde{\chi} \rightarrow \infty$.

Qualitative comparisons were made between (a) the cone surface pressure and skin friction calculated in the present program, and predictions of hypersonic interaction theory, and (b) the base pressure distribution computed for the separated field, and corresponding experimental data for flat-based cones. The AFTON surface pressure and skin-friction distributions, shown in Figure 33, decrease with increasing Reynolds number. Since the hypersonic interaction parameter, χ , is inversely proportional to $R_e^{\frac{1}{2}}$ at constant free-stream Mach number, χ is greater for the lower-Reynolds-number flow field. Therefore, the calculated surface pressure and skin-friction distributions decrease with decreasing values of χ , in accord with weak-interaction theory.²⁶

The computed base-pressure distributions at Reynolds numbers 735 and 4150 are shown in Figure 34; the ordinate of the figure is the base circumferential angle, θ_b , measured counterclockwise from the system axis. In the lower-Reynolds-number case, where no flow separation occurred, a large pressure rise was found near $\theta_b = 47^\circ$ as a result of the collision of plume and airstream gases. For the high-Reynolds-number flow, boundary layer separation on the spherical after-body produced a rapid rise in both the plume and external airstream pressures to a nearly constant pressure plateau in the separation region; the domain of constant pressure extended from $\theta_b = 35^\circ$ to $\theta_b = 70^\circ$. A similar regime of constant pressure was measured on the flat-based cone tested by Boger, Rosenbaum and Reeves⁶ at Mach 10, Reynolds number $1.34 \cdot 10^5$, $\alpha = 0^\circ$, and $p_c/p_\infty = 1.7 \cdot 10^6$ (Figure 35).

6. SUMMARY AND CONCLUSIONS

The AFTON 2A computer code has been used to calculate two complete hypersonic plume-body flow fields. Although the two flows differ only in Reynolds number, and then by a factor less than six, the computed flow-field structures are very different. While no flow separation is observed at a Reynolds number of 735, the cone and after-body boundary layers both separate at a Reynolds number of 4150, yielding a separation bubble and a complicated system of shock waves. Thus, the results indicate that the structure of hypersonic-plume-interaction flow fields varies greatly over the Reynolds-number range spanned in this study, and the determination of flow field structure must therefore be considered part of the total problem of flow field prediction.

Two further conclusions related to the interaction of a jet plume with a hypersonic airstream have been drawn in this study. First, based on the evidence provided by the two numerical flow fields, heat conduction effects cannot be neglected in the plume, even in the inner core. Secondly, despite the sensitivity of the near field to Reynolds number, and the larger plume size calculated relative to the Jarvinen and Hill prediction, scaling of the plume shock and dividing streamline radii with Reynolds number are consistent with the Jarvinen-Hill scaling law.

The second point should be further verified for different flight conditions and geometries; such a viscous scaling law, if generally valid, might serve as a check for existing hypersonic-free-stream plume interaction models. However,

the first point is at wide variance with other hypersonic plume theories, and is sufficiently important to merit future study; it must be emphasized that the effects of a non-isentropic inner core extend far beyond the near field, and have a marked effect (for example) on the Mach disc.

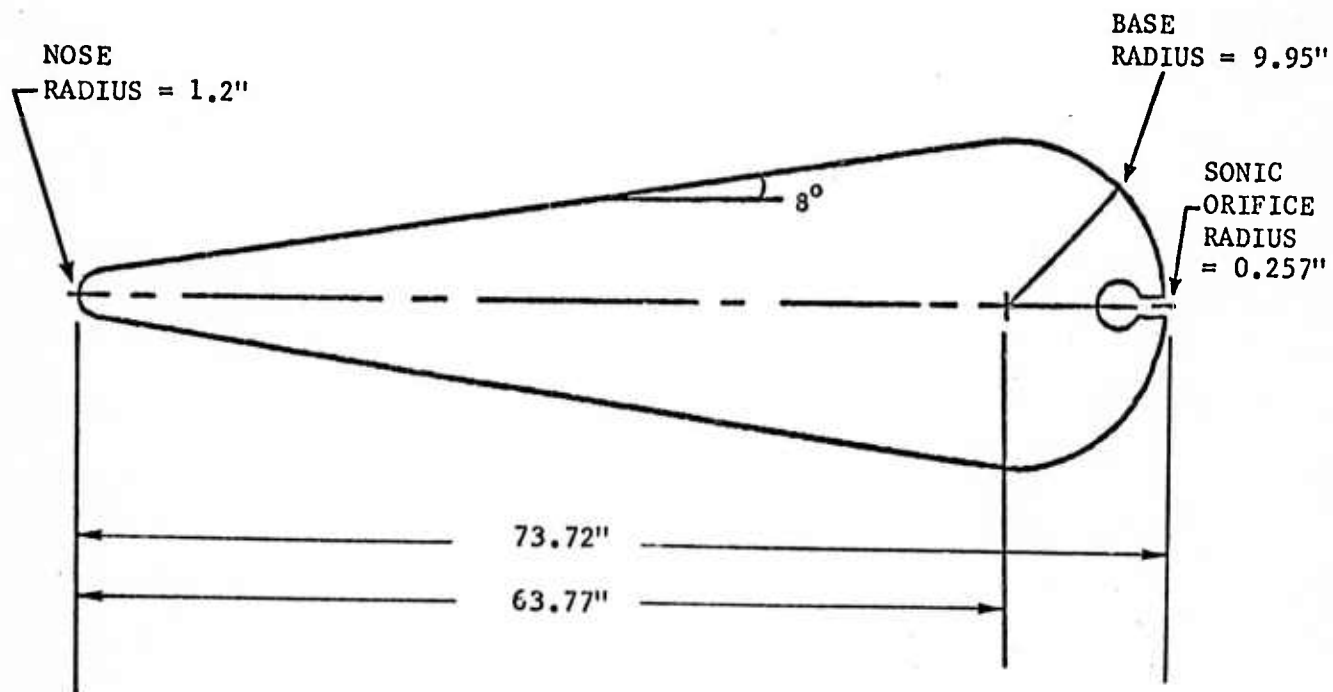


Figure 1. Blunt-nosed cone with a spherical after body.

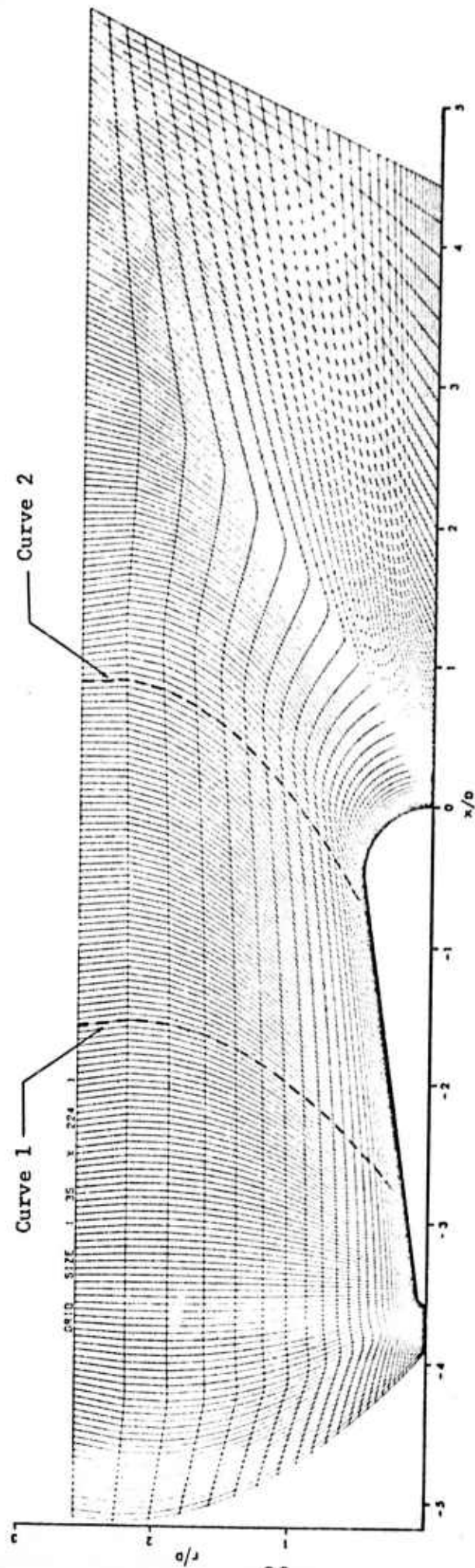


Figure 2. Finite-difference mesh used in the separation-free plume calculation; dashed lines indicate upstream boundary locations for reduced-mesh calculations.

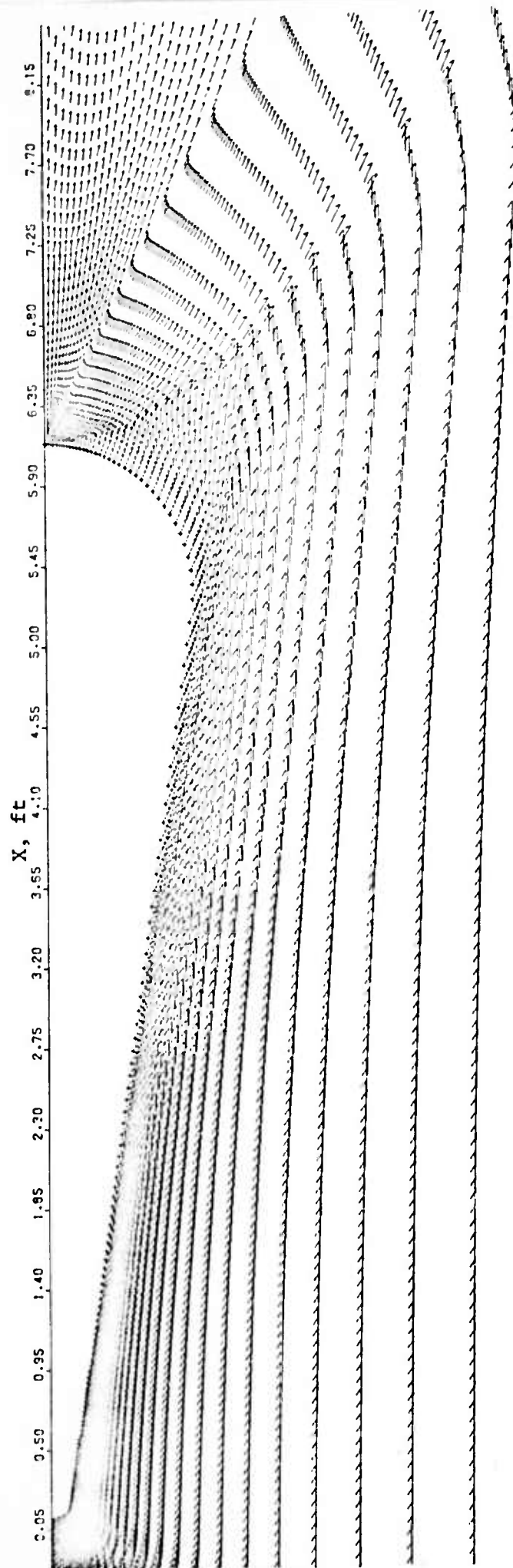


Figure 3. Velocity vector plot of the initial flow field for the separation-free-plume calculation (Problem 563.0).

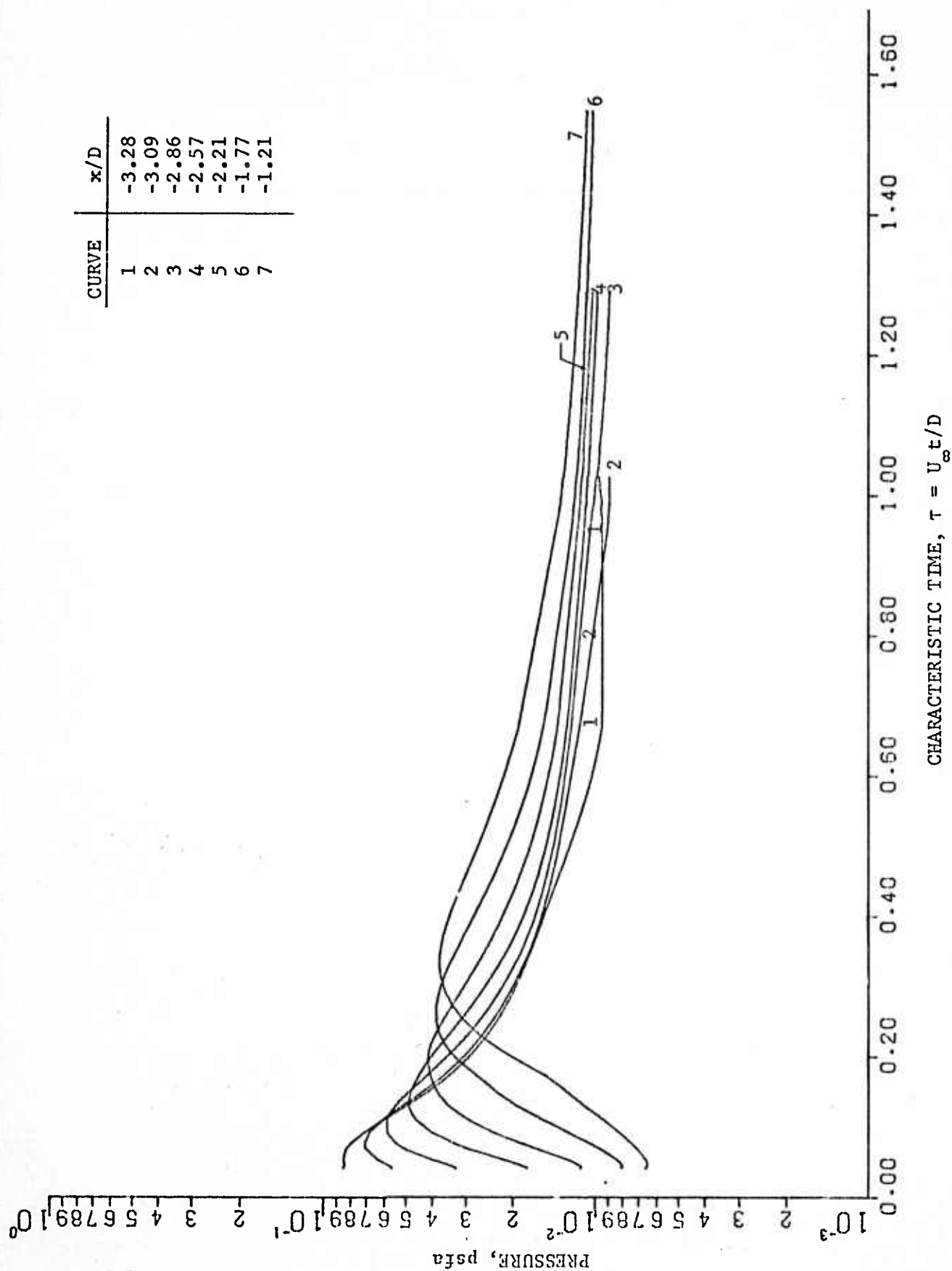


Figure 4. Variation of pressure with time along the cone surface for the separation-free plume calculation.

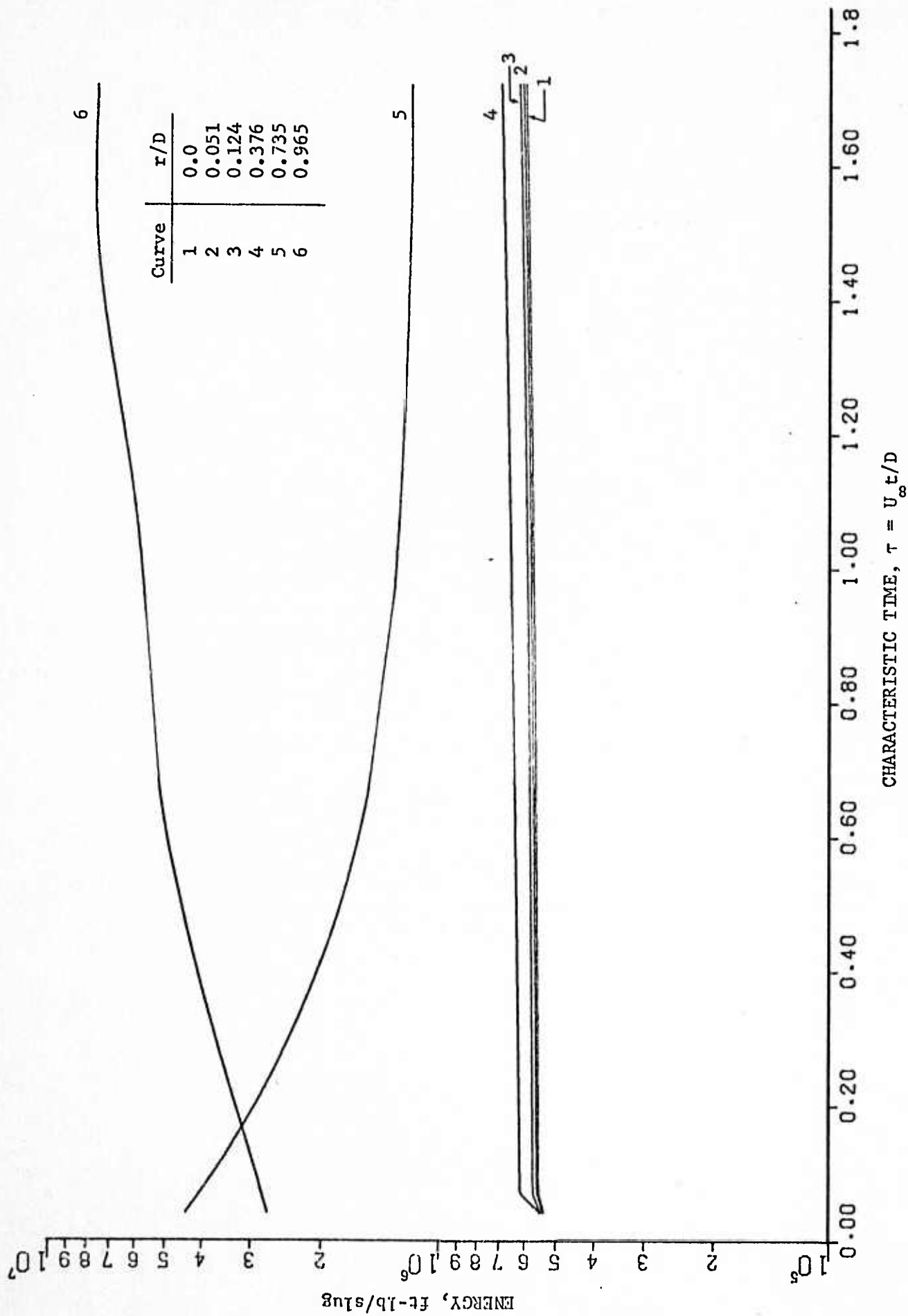


Figure 5. Variation of specific internal energy with time at a station 1.725 base diameters downstream of the body for the separation-free plume calculation.

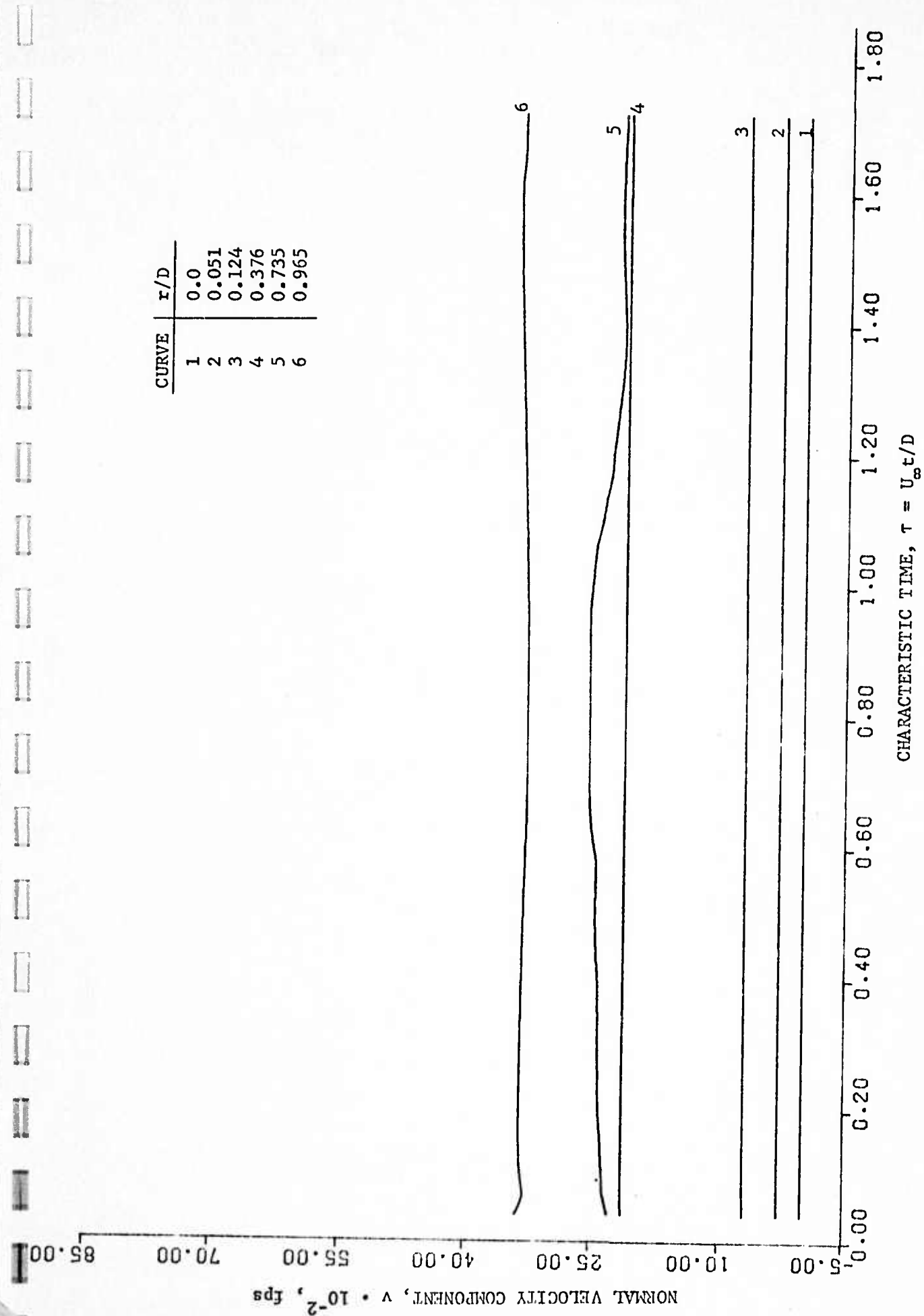


Figure 6. Variation of the normal component of velocity with time at a station of 1.725 base diameters downstream of the body for the separation-free plume calculation.

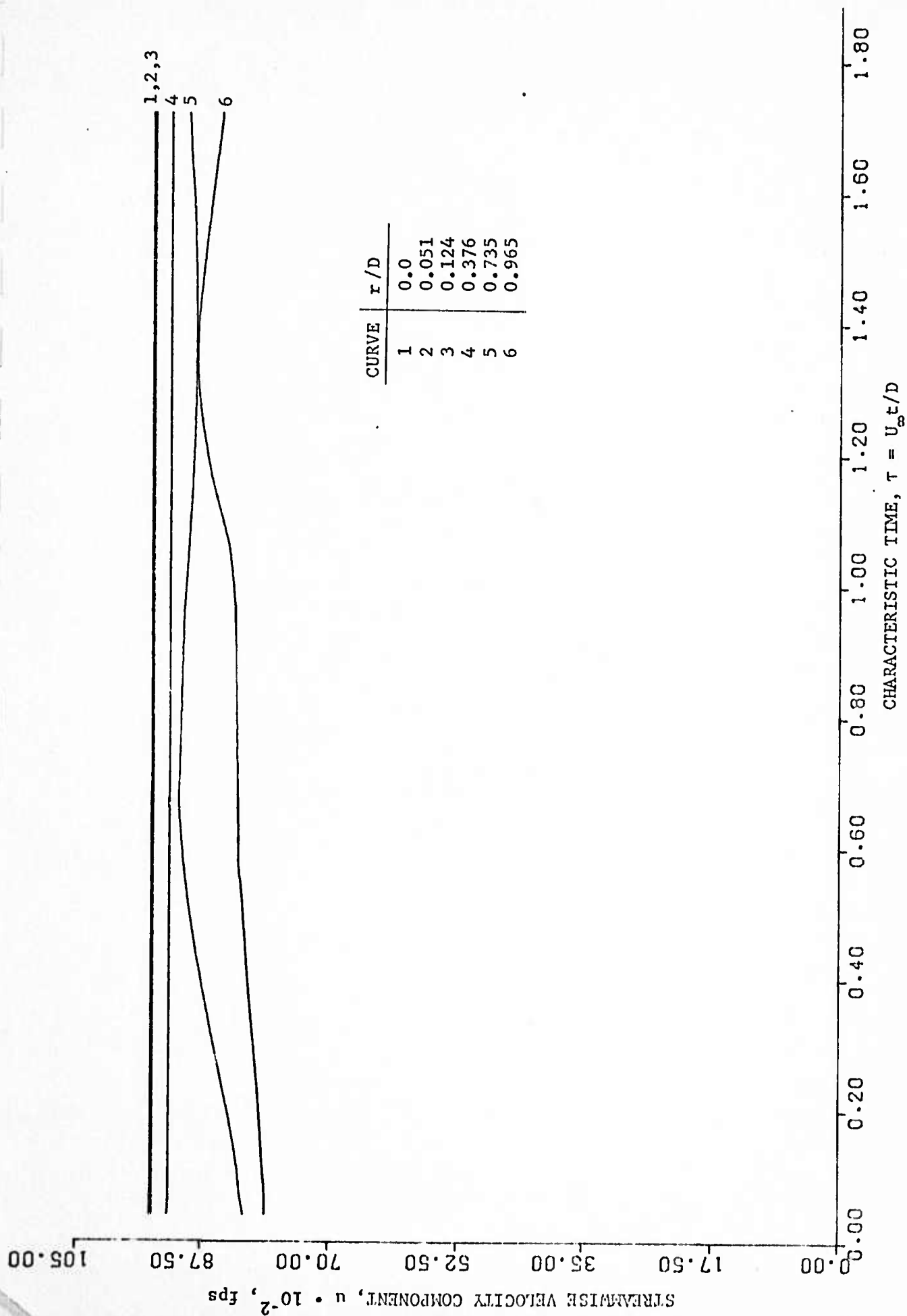


Figure 7. Variation of the streamwise component of velocity with time at a station of 1.725 base diameters downstream of the body for the separation-free plume calculation.

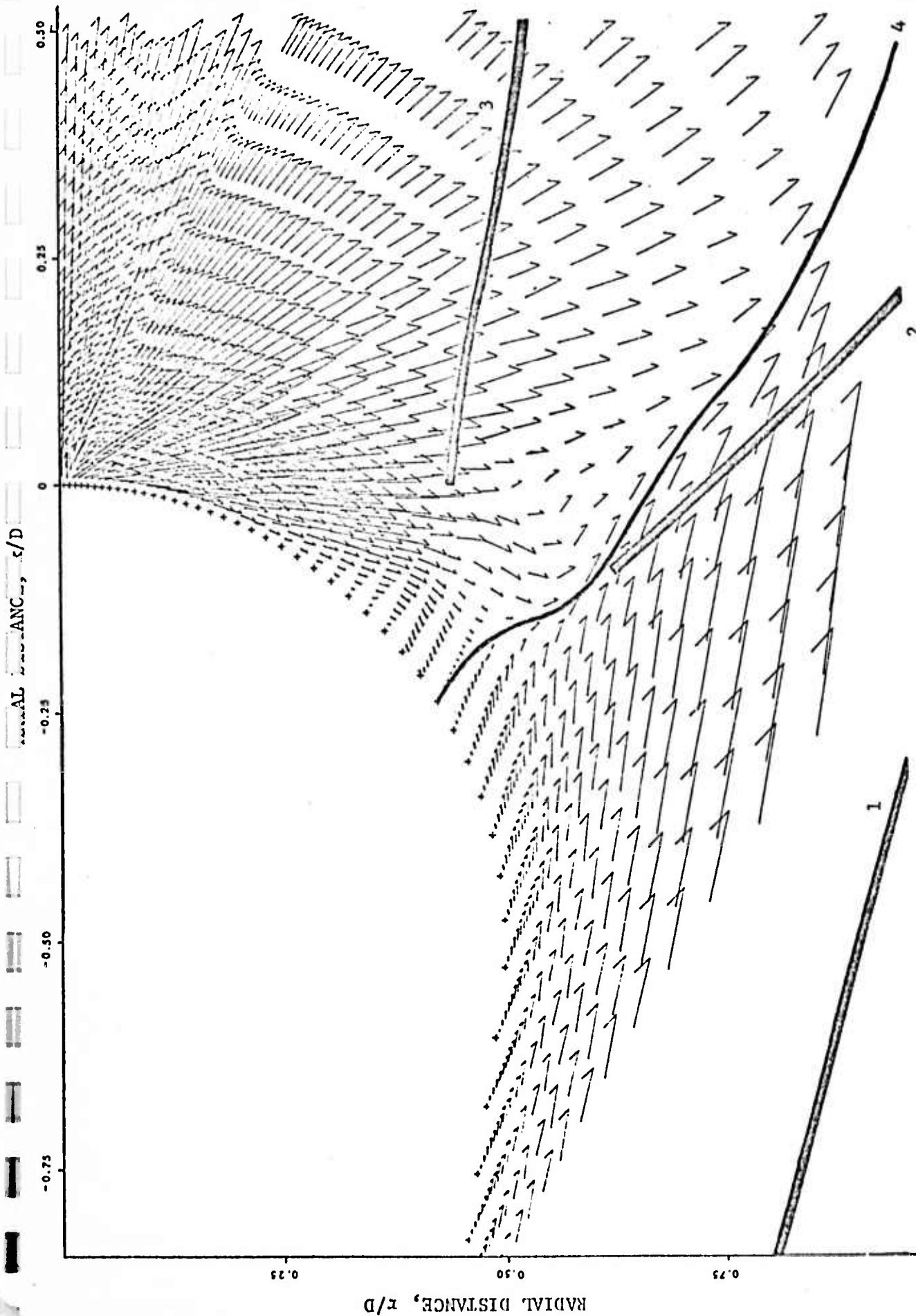


Figure 8. Velocity vector plot of the base flow field for the separation-free plume calculation; Mach 26; Reynolds number 735; mass injection rate 0.15 lb/sec; Curves 1, 2 and 3 denote the cone, plume, and inner shocks; Curve 4 denotes the dividing streamline.

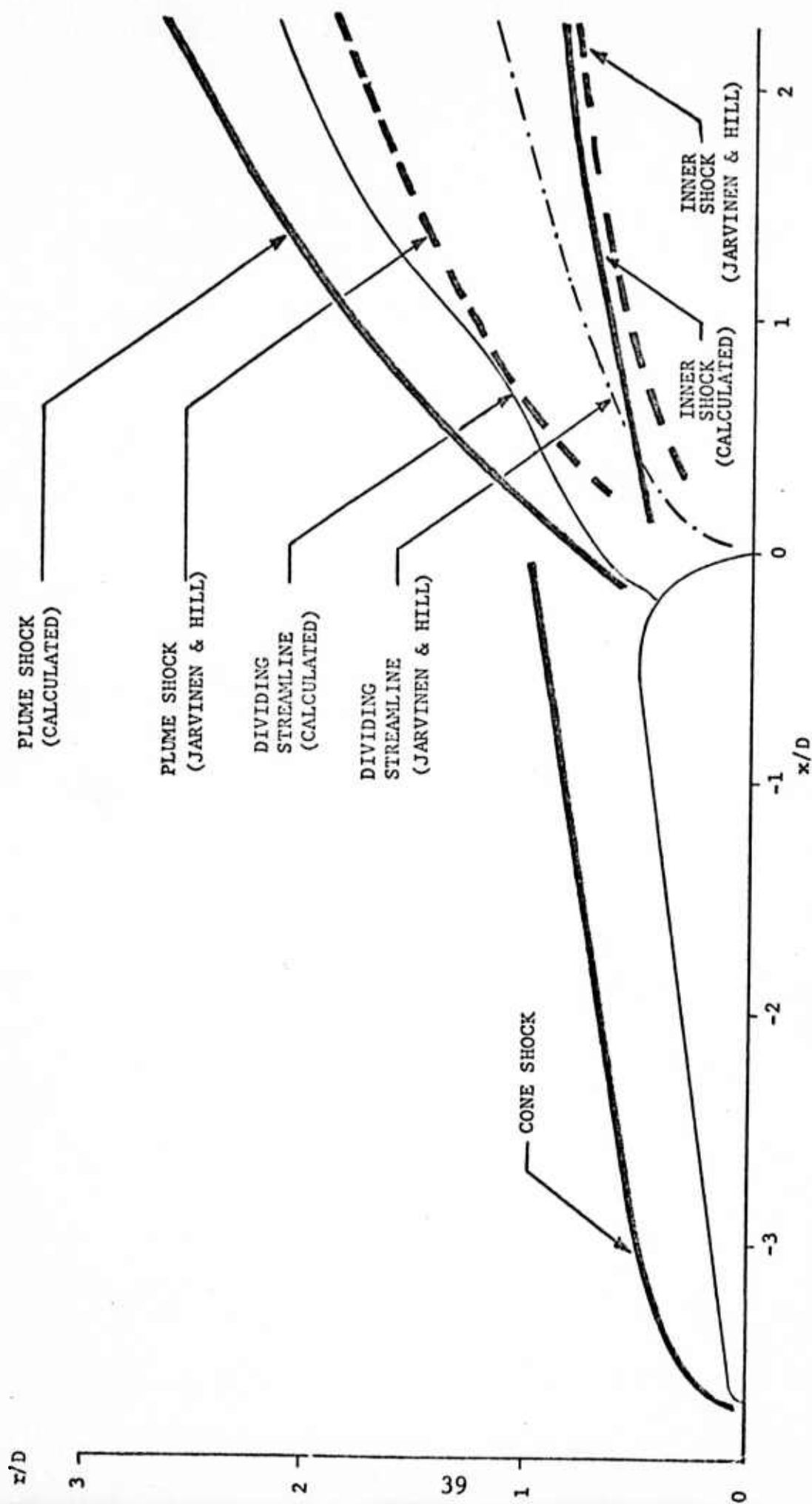


Figure 9. Near field structure for flow past the conical body at a Reynolds number of 735, including the calculated cone shock, plume shock, inner shock and dividing streamline; the plume shock, inner shock and dividing streamline as determined from the characteristics correlation of Jarvinen and Hill are shown for comparison.

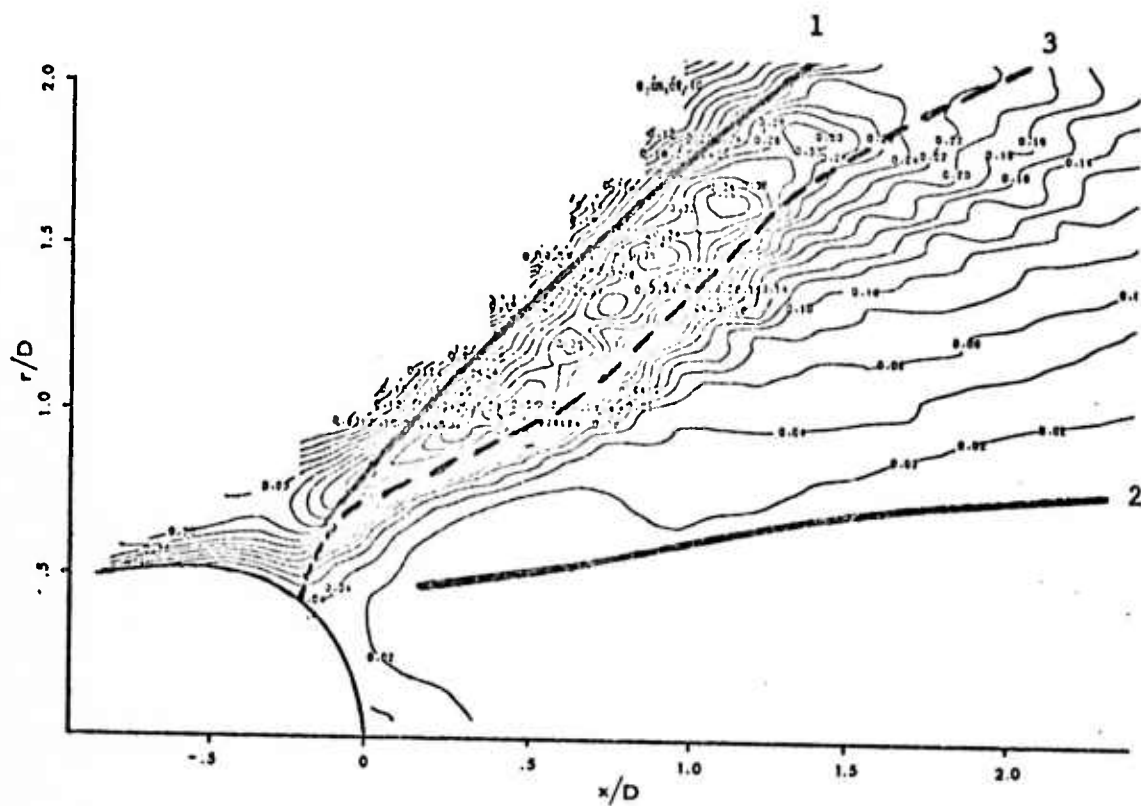


Figure 10. Internal energy contours of the flow field downstream of the base for the separation-free plume calculation. The contour parameter is internal energy nondimensionalized by the free-stream stagnation internal energy; Curves 1, 2 and 3 denote the locus of the plume shock, inner shock, and dividing streamline.

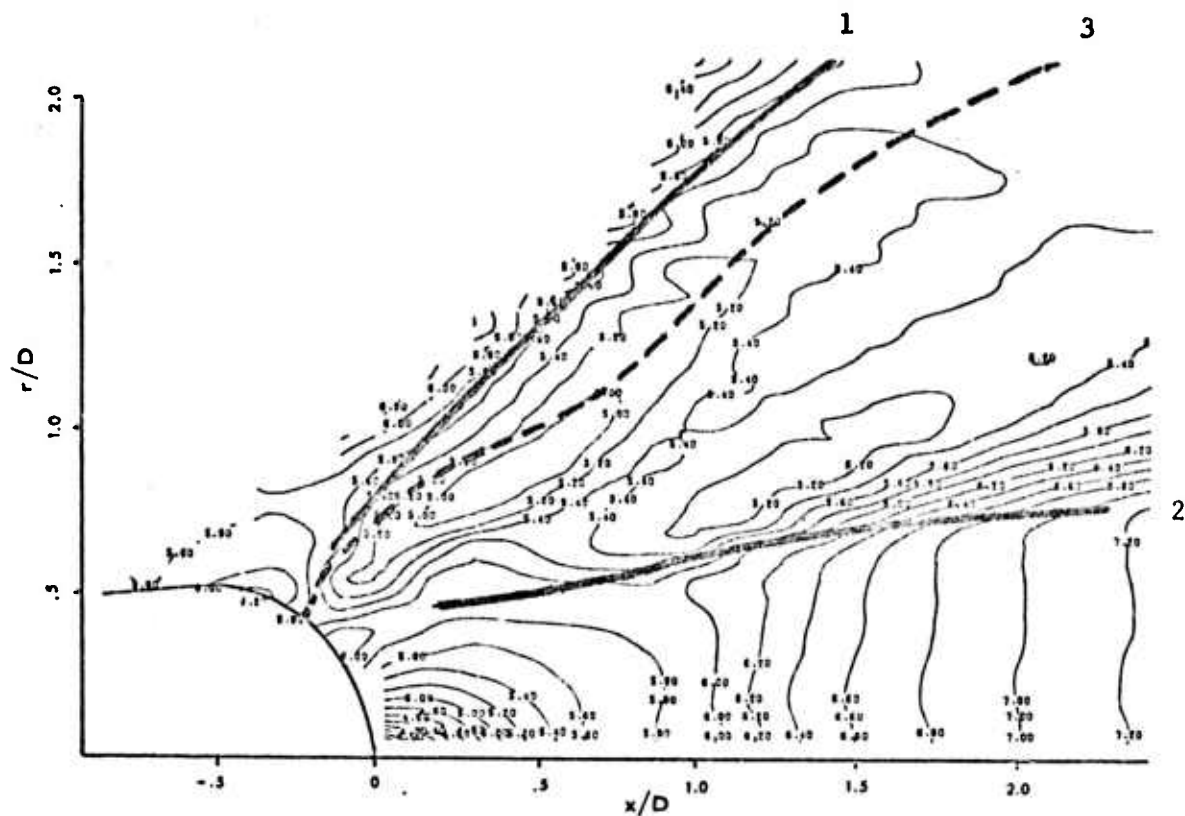


Figure 11. Pressure contours of the flow field downstream of the base for the separation-free plume calculation; the contour parameter, Z , is defined as $Z = |\log_{10} (p/p_{t\infty})|$, where $p_{t\infty}$ is the free-stream stagnation pressure; Curves 1, 2, and 3 denote the locus of the plume shock, inner shock, and dividing streamline.

Reproduced from
best available copy.

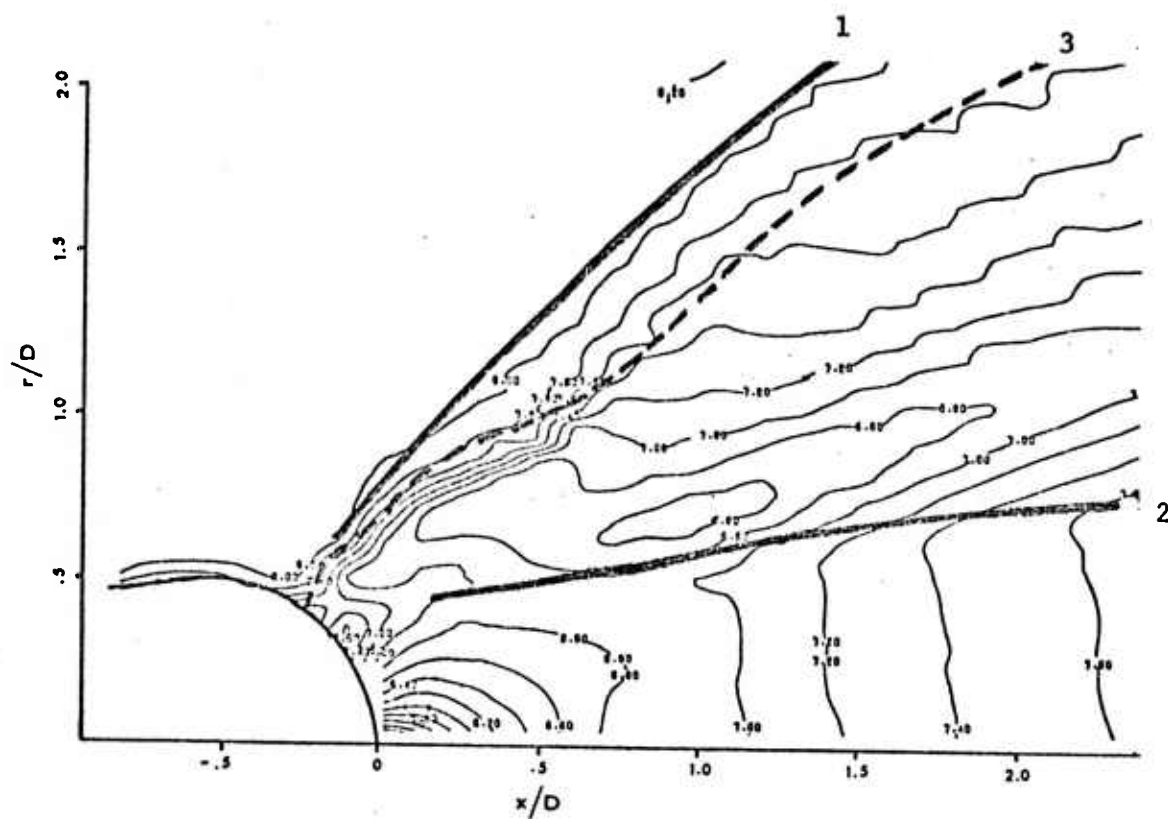


Figure 12. Density contours of the flow field downstream of the base for the separation-free plume calculation; the contour parameter, Z , is defined as $Z = |\log_{10} \rho|$; Curves 1, 2, and 3 denote the locus of the plume shock, inner shock, and dividing streamline.

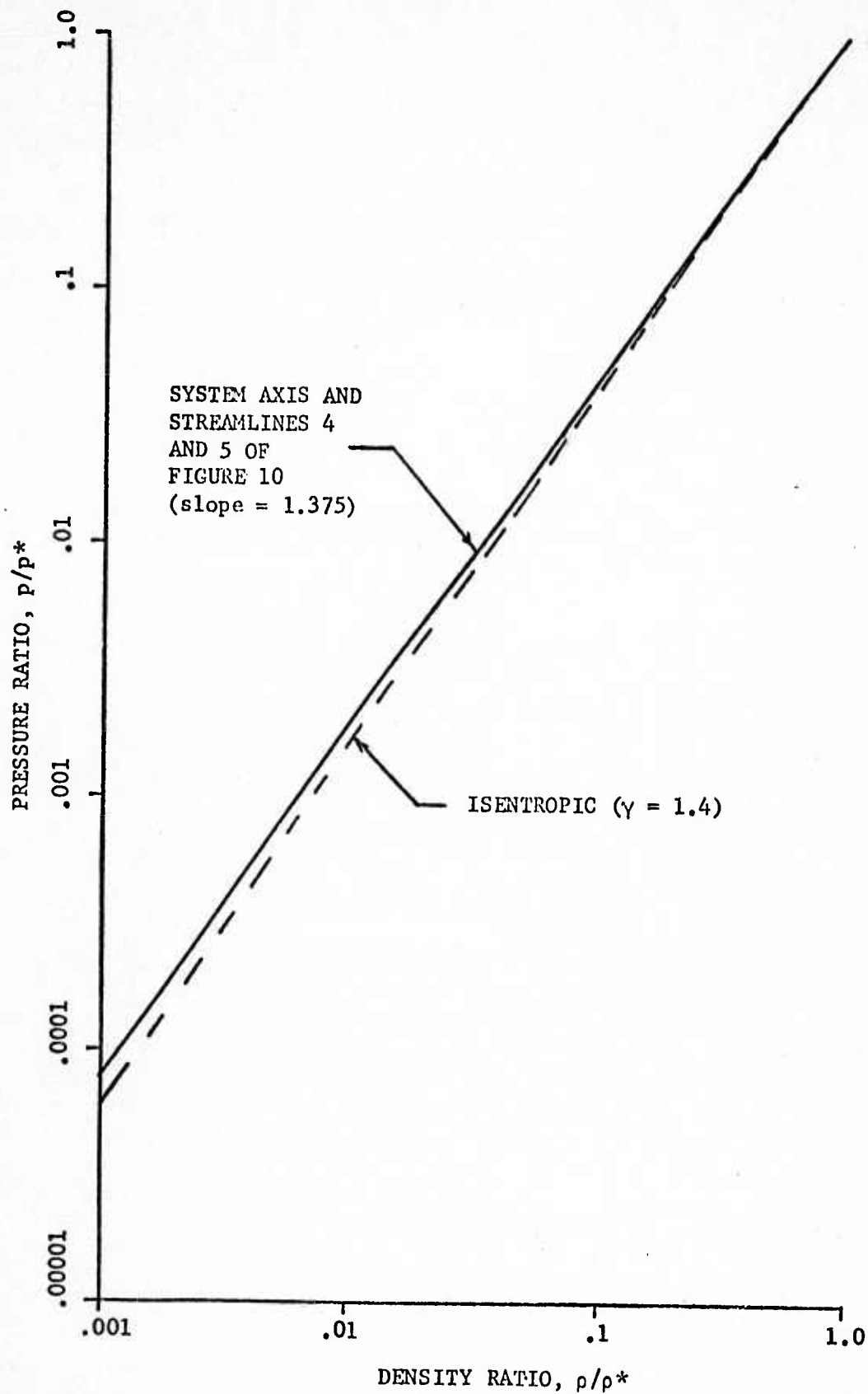
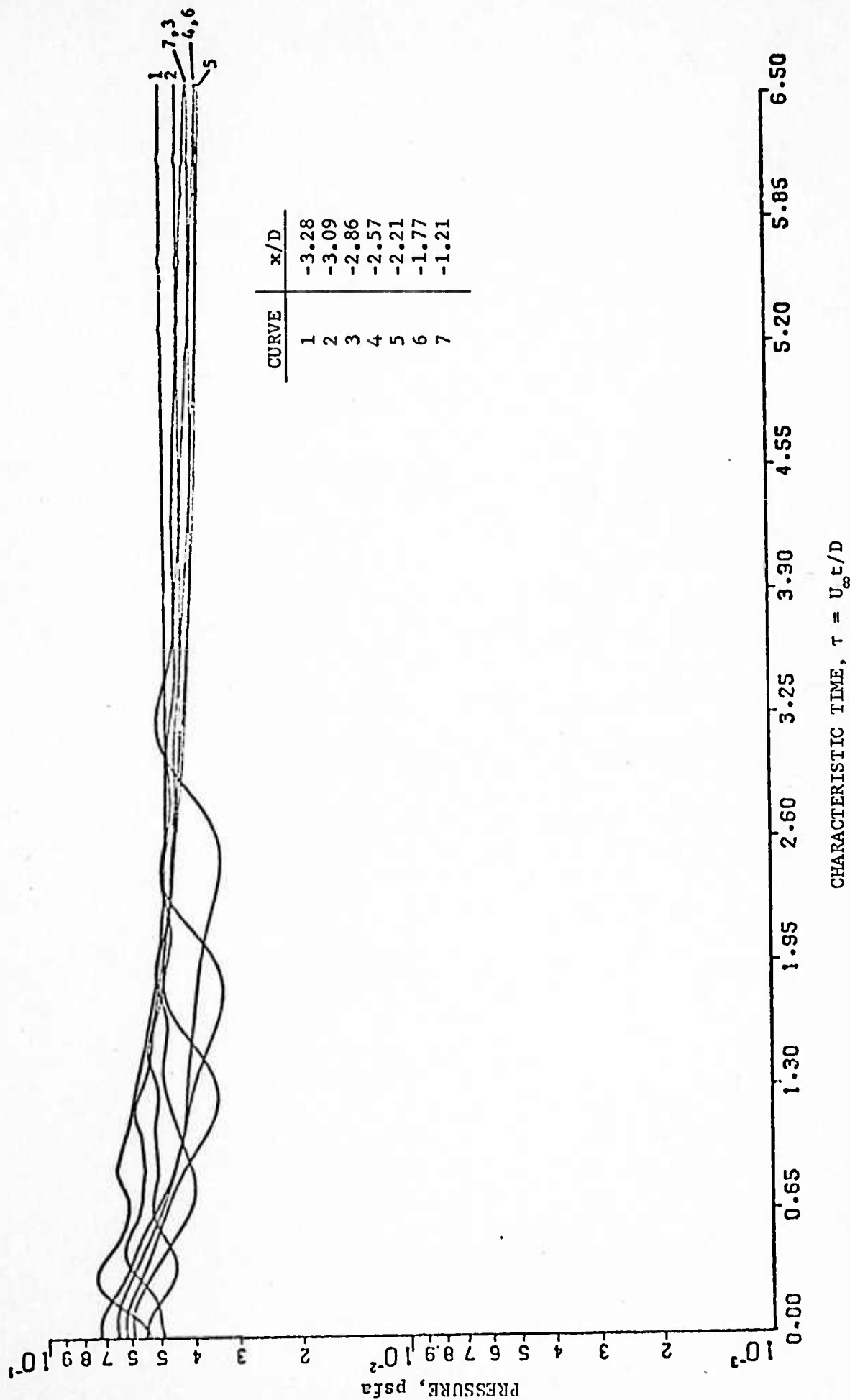


Figure 14. Variation of pressure with density along streamlines in the plume inner core for the separation-free plume calculation.



CHARACTERISTIC TIME, $\tau = U_{\infty} t / D$

Figure 15. Variation of pressure with time along the cone surface for the separation plume calculation for step one.

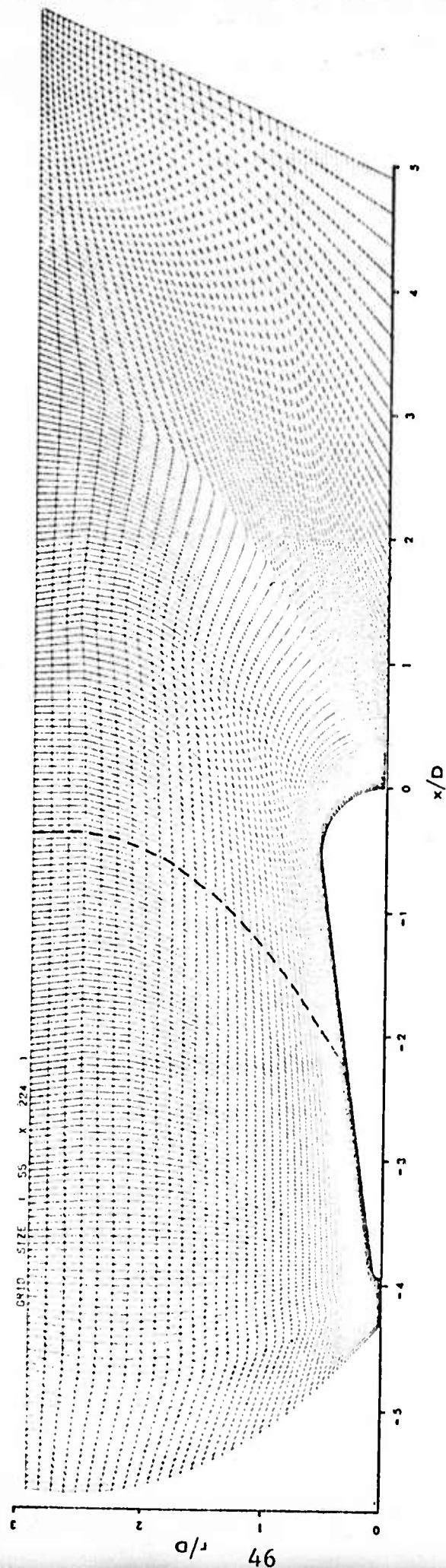


Figure 16. Finite difference mesh used in the separation plume calculation; the dashed line indicates the upstream boundary location for the reduced mesh calculation.

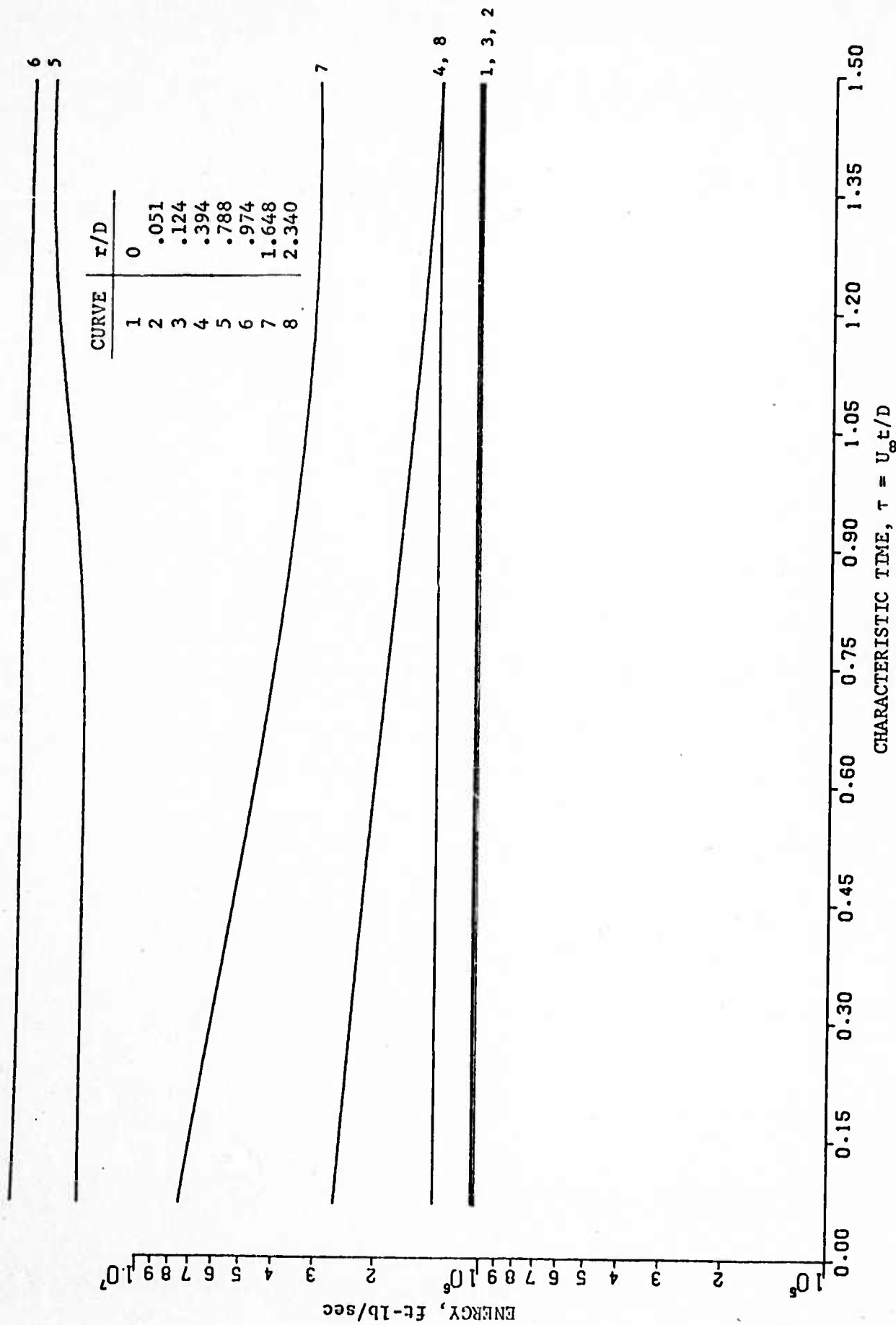


Figure 17. Variation of specific-internal energy with time at a station of 1.56 base diameters aft of the body for the separation plume calculation for step three.

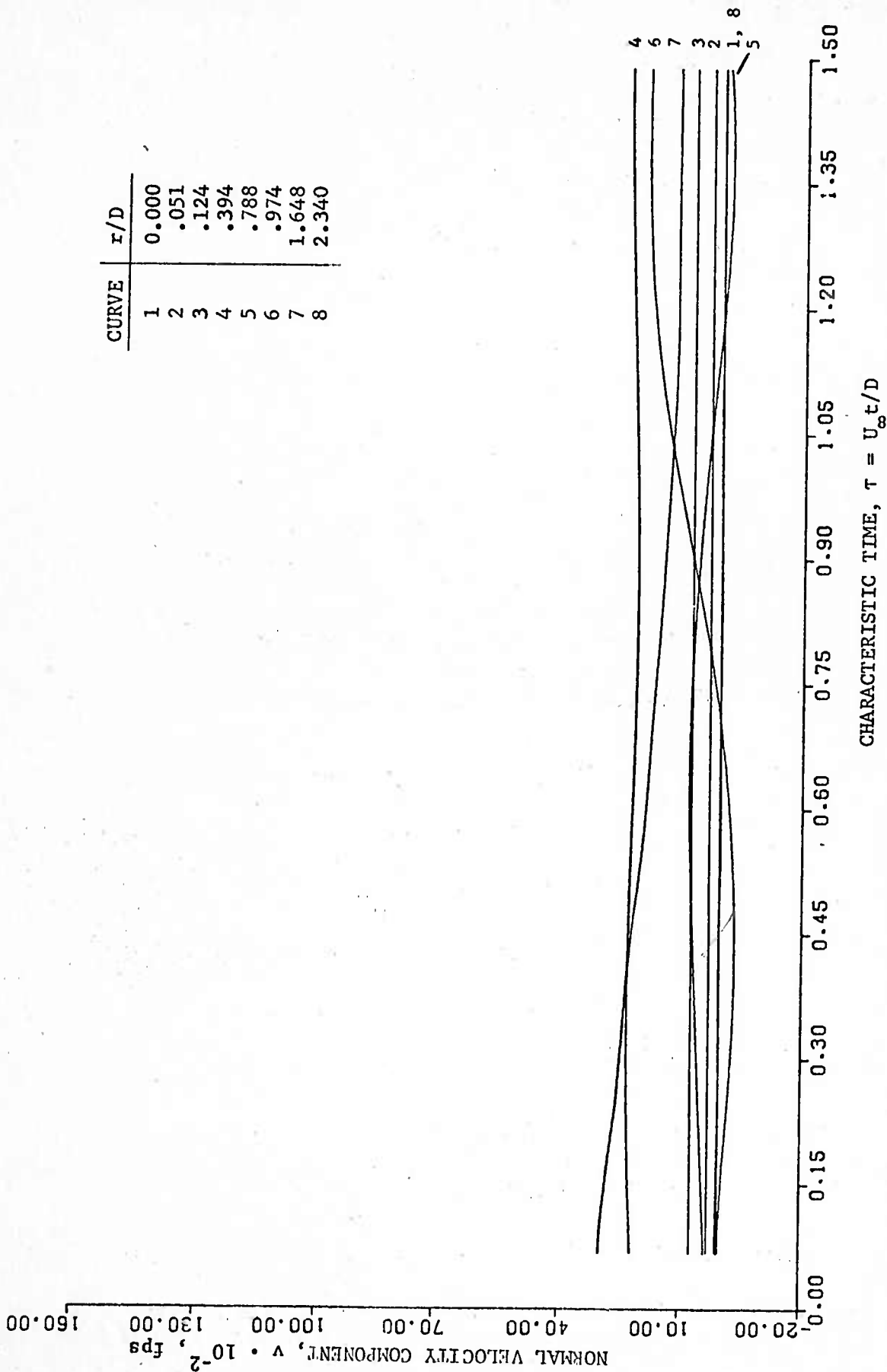


Figure 18. Variation of the normal velocity component with time at a station 1.56 base diameters downstream of the body for the separation plume calculation for step three.

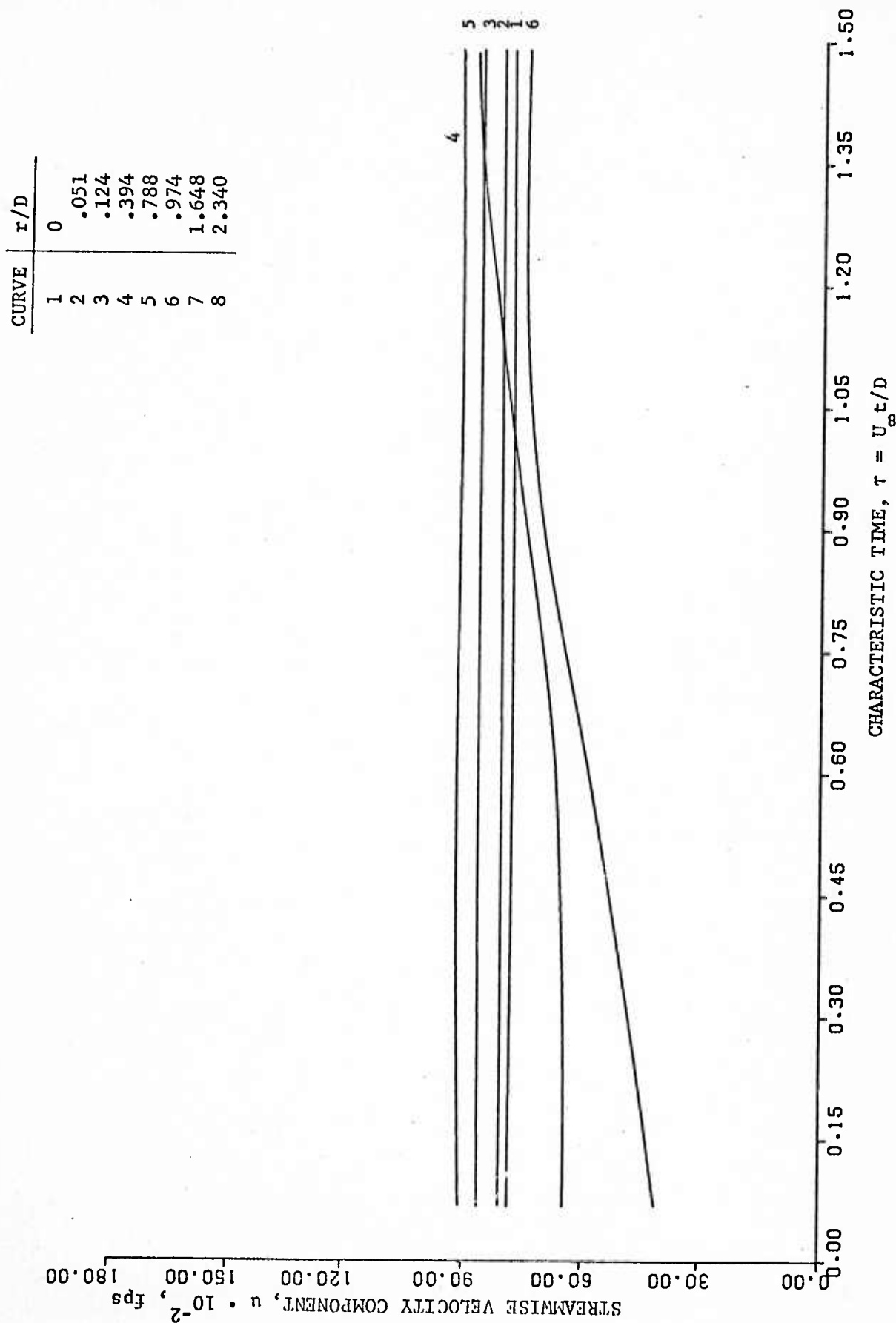


Figure 19. Variation of the streamwise component of velocity with time at a station of 1.56 base diameters aft of the body for the separation plume calculation for step three.

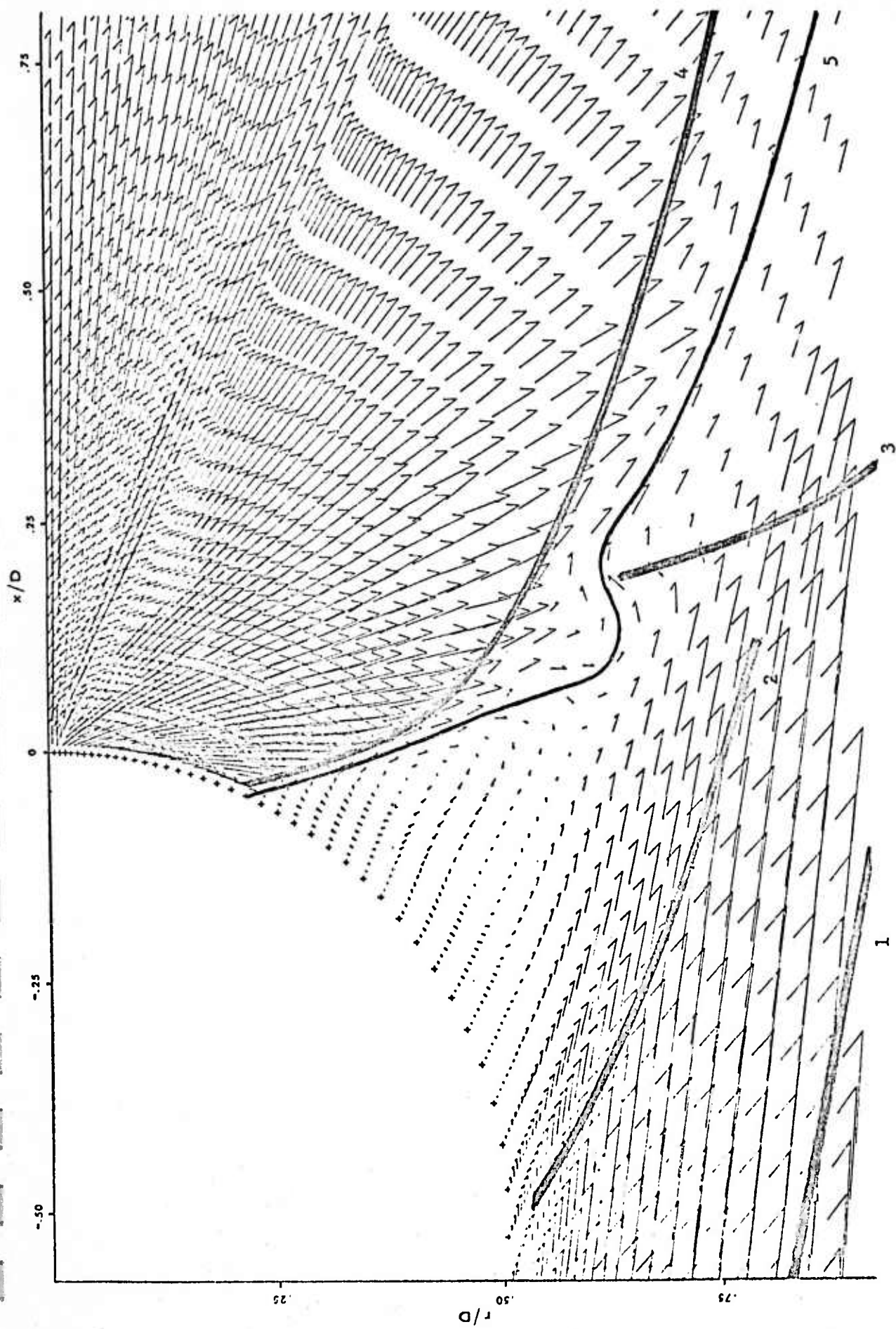


Figure 20. Velocity vector plot of the base flow field for the separation plume calculation; Mach 26; Reynolds number 4150; mass injection rate 0.15 lb/sec. Curves 1, 2, 3 and 4 denote the cone, cone separation, plume and plume separation shocks; Curve 5 denotes the dividing streamline.

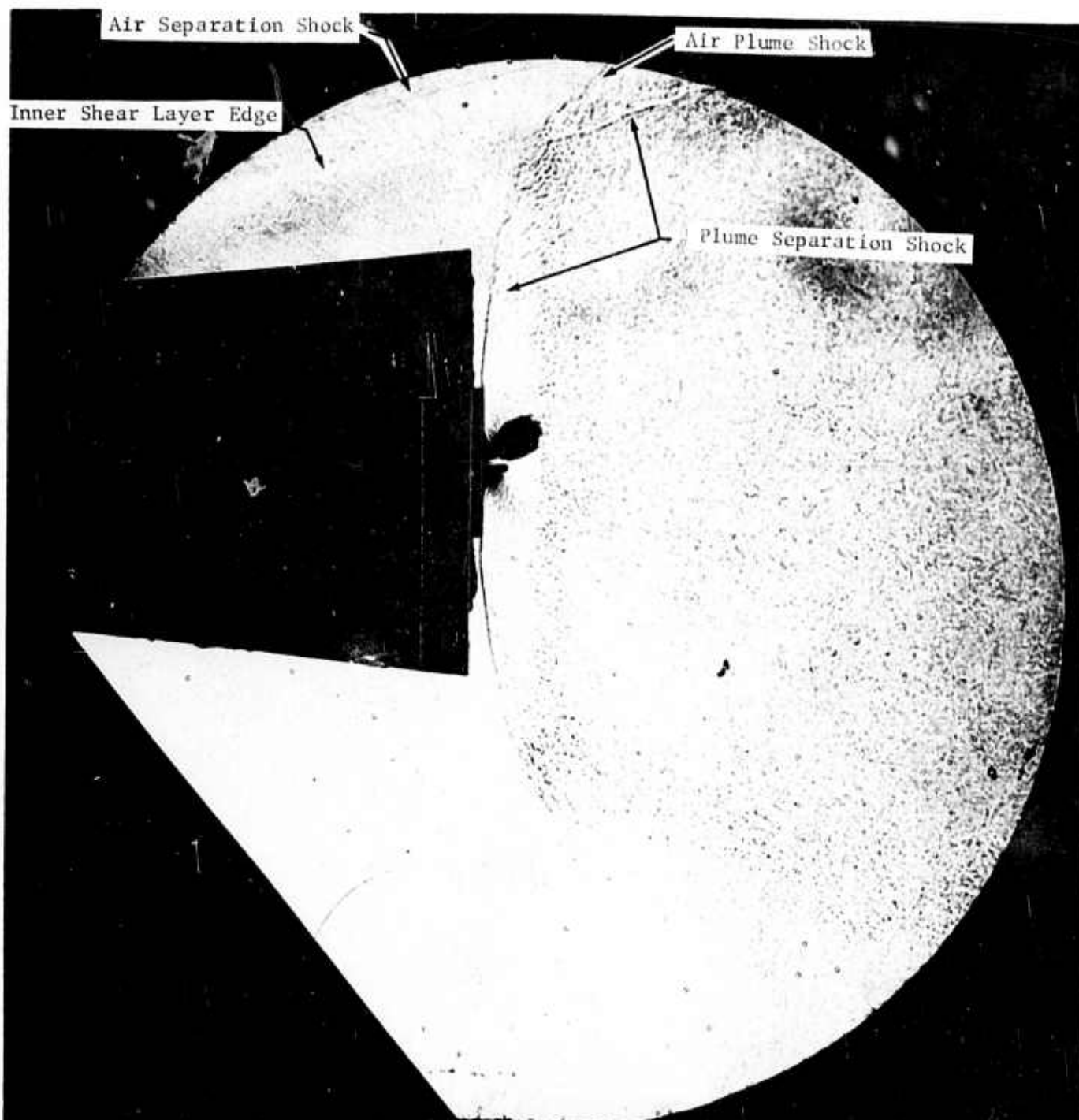


Figure 21. Shadowgraph of the plume-external airstream interaction region with plume-induced separation on the cone; $\alpha = 0^\circ$; $R_{e_\infty}/ft = 2.5 \times 10^5$, $M_\infty = 10$, $P_c/P_\infty = 1.72 \times 10^5$.

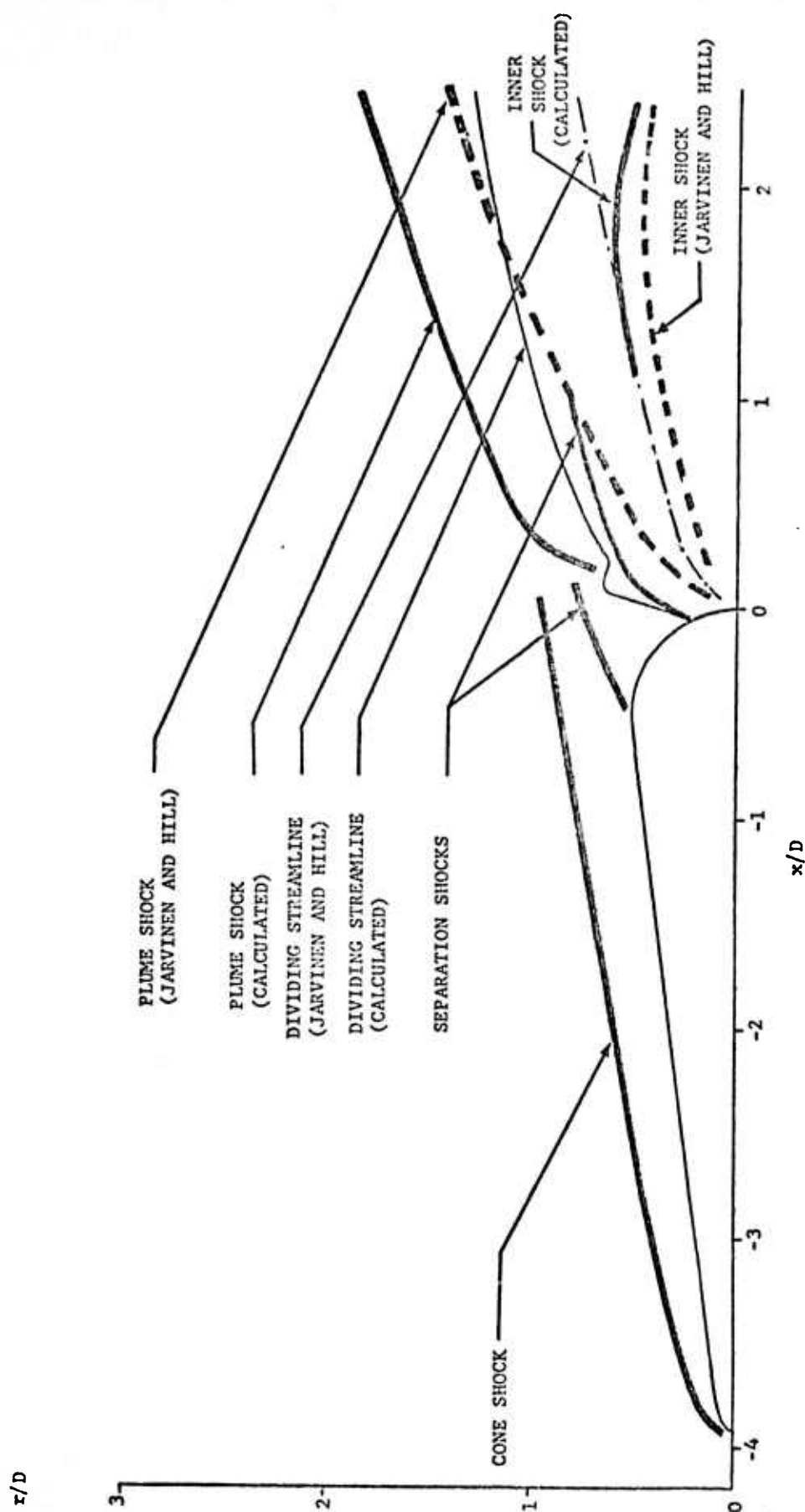


Figure 22. Near field structure for flow past the conical body at a Reynolds number of 4150, including the calculated cone shock, plume shock, inner shock and dividing streamline; the plume shock, inner shock and dividing streamline as determined from the characteristics correlation of Jarvinen and Hill are shown for comparison.

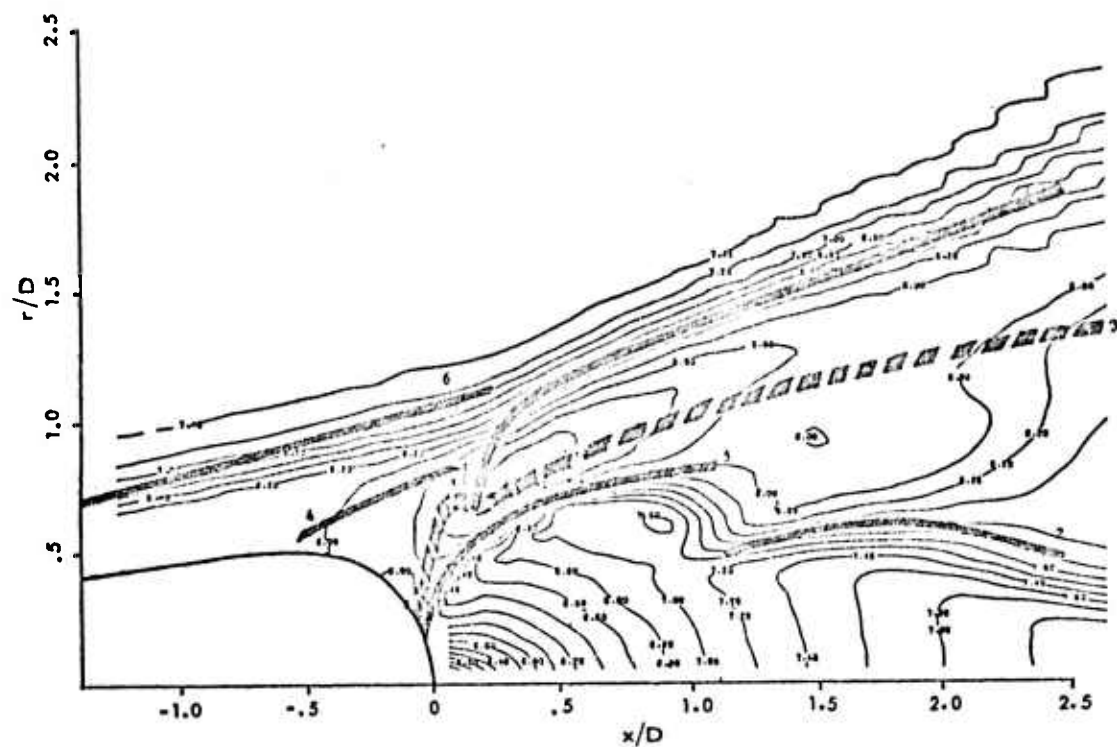


Figure 24. Pressure contours of the flow field downstream of the base for the separation plume calculation. The contour parameter Z is defined as $Z = \log_{10} (p/p_{t\infty})$, where $p_{t\infty}$ is the free stream stagnation pressure; Curves 1, 2 and 3 denote the locus of the plume shock, inner shock and dividing streamline, respectively; Curves 4 and 5 denote the separation shocks; Curve 6 denotes cone shock.

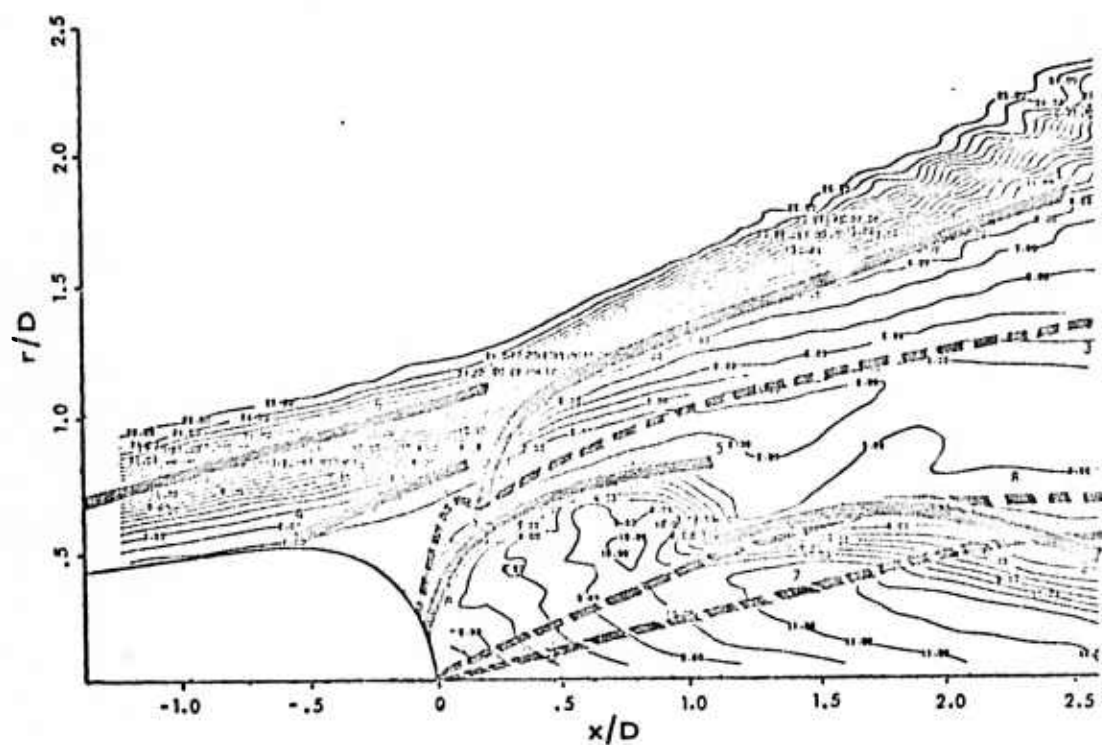


Figure 26. Mach-number contours of the flow field downstream of the base for the separation plume calculation. Curves 1, 2 and 3 denote the locus of the plume shock, inner shock, and dividing streamline, respectively; Curves 4 and 5 denote the separation shock; Curve 6 denotes the cone shock; Curves 7 and 8 denote streamlines in the plume inner core.

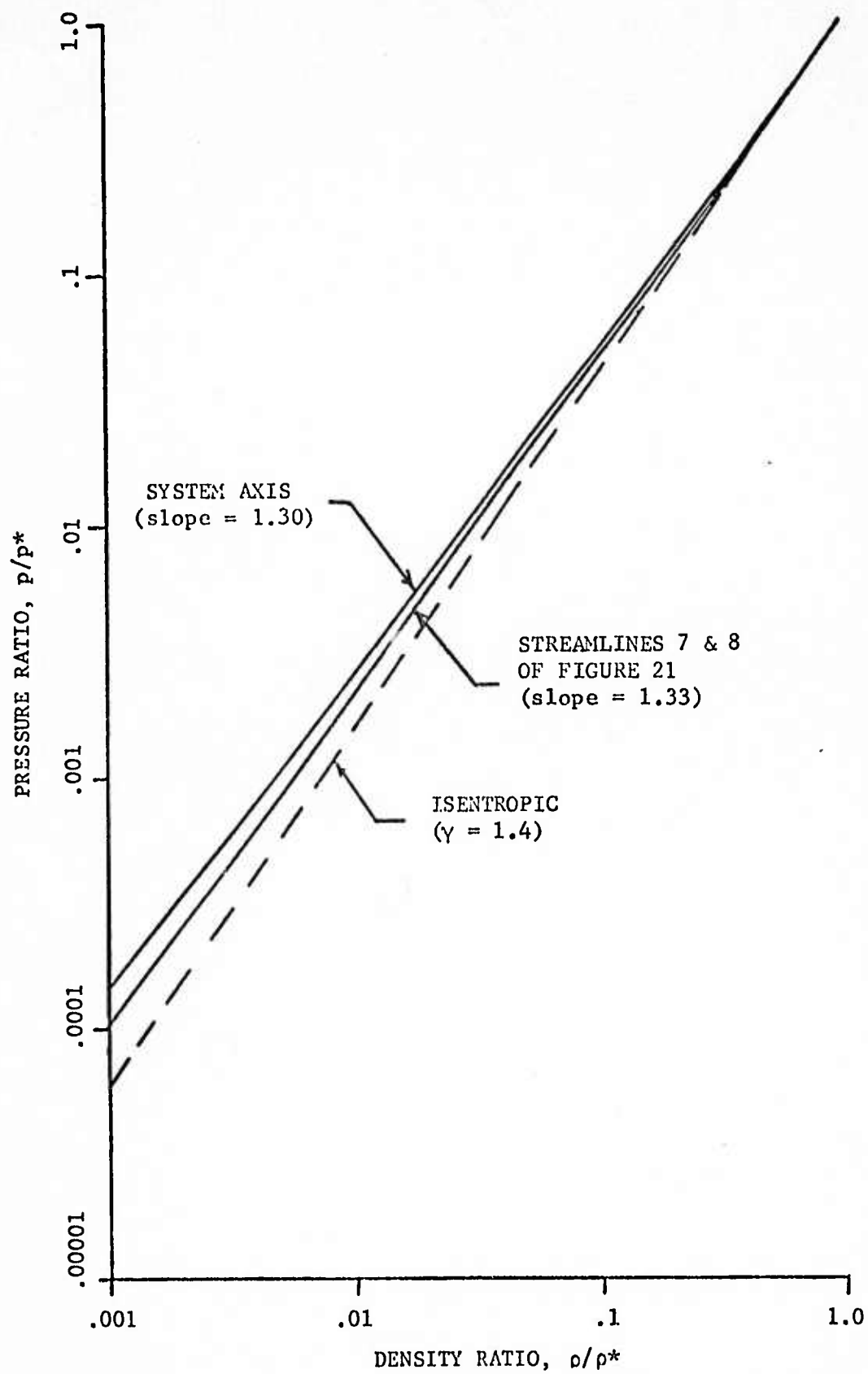


Figure 27. Variation of pressure with density along streamlines in the plume inner core for the separation plume calculation.

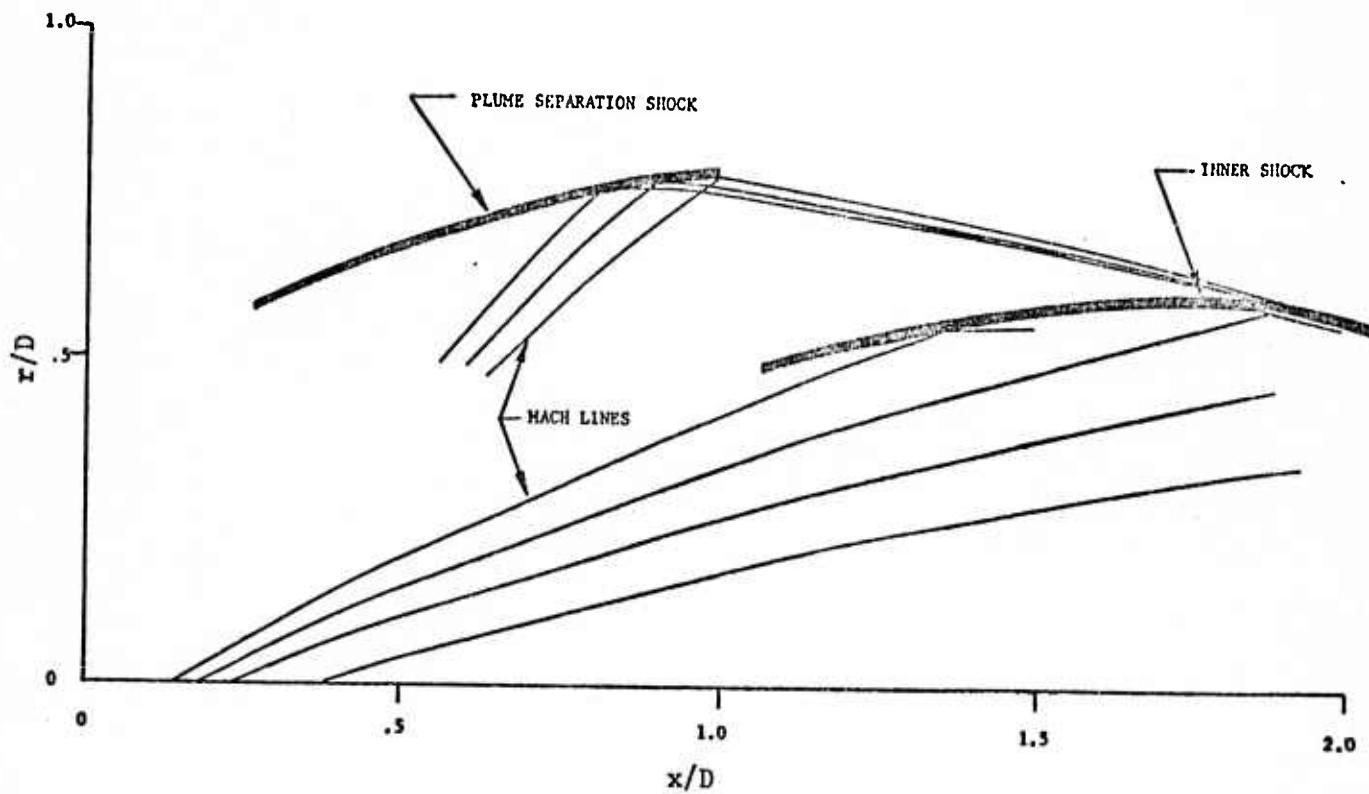


Figure 28. Mach lines in the vicinity of the plume separation shock and inner shock.

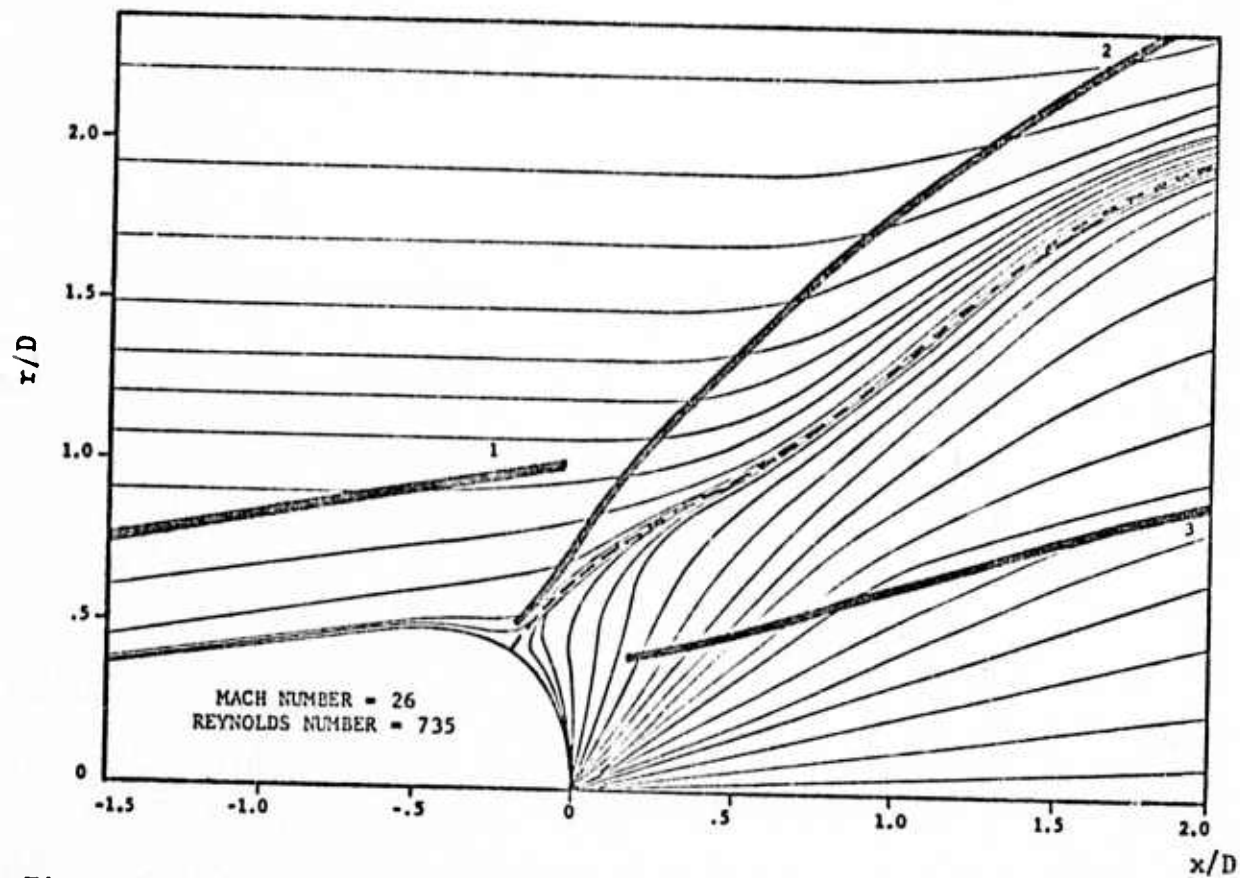
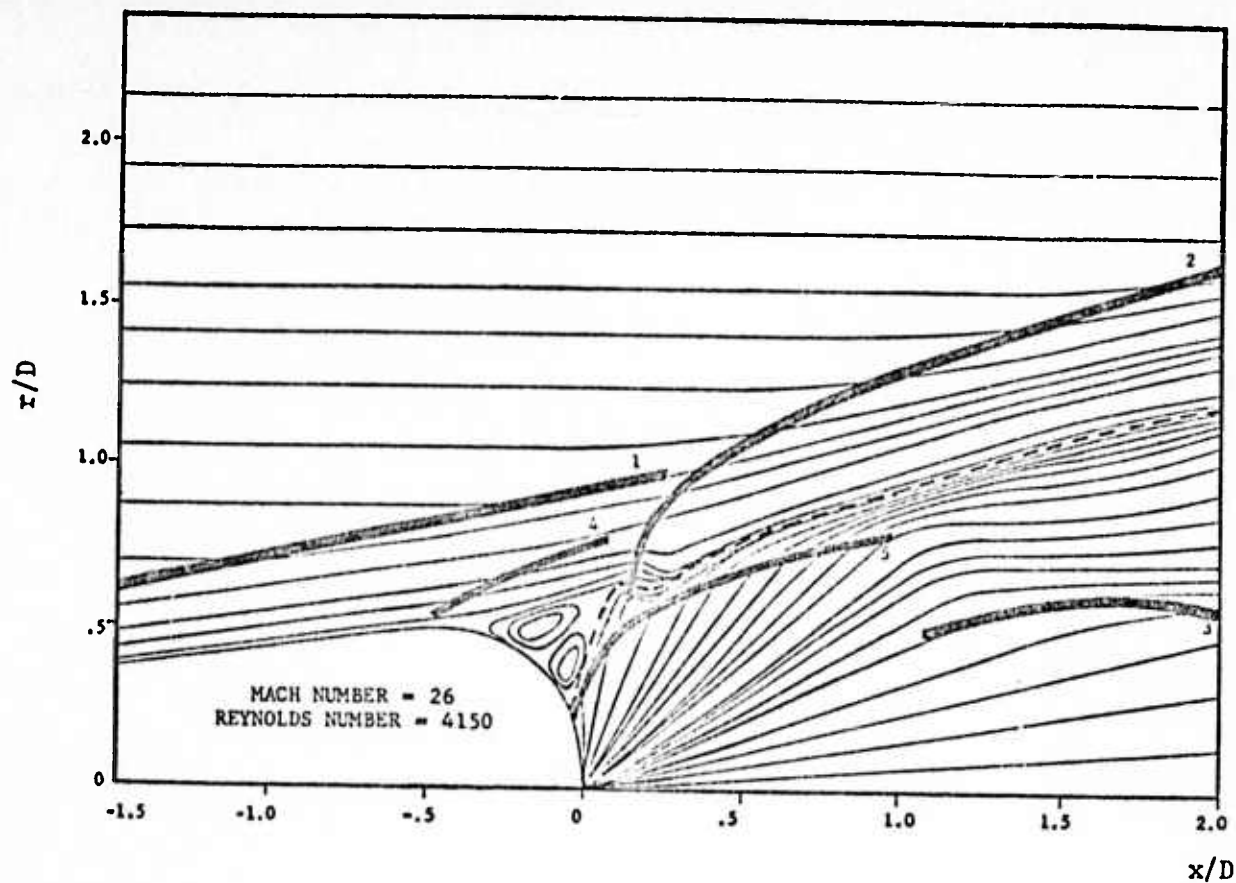


Figure 29. Streamlines for the two calculated flow fields; Curves 1, 2 and 3 denote cone, plume and inner shock, respectively; Curves 4 and 5 indicate airstream separation and plume separation shock, respectively; dashed lines show the dividing streamline.

Reproduced from
best available copy.

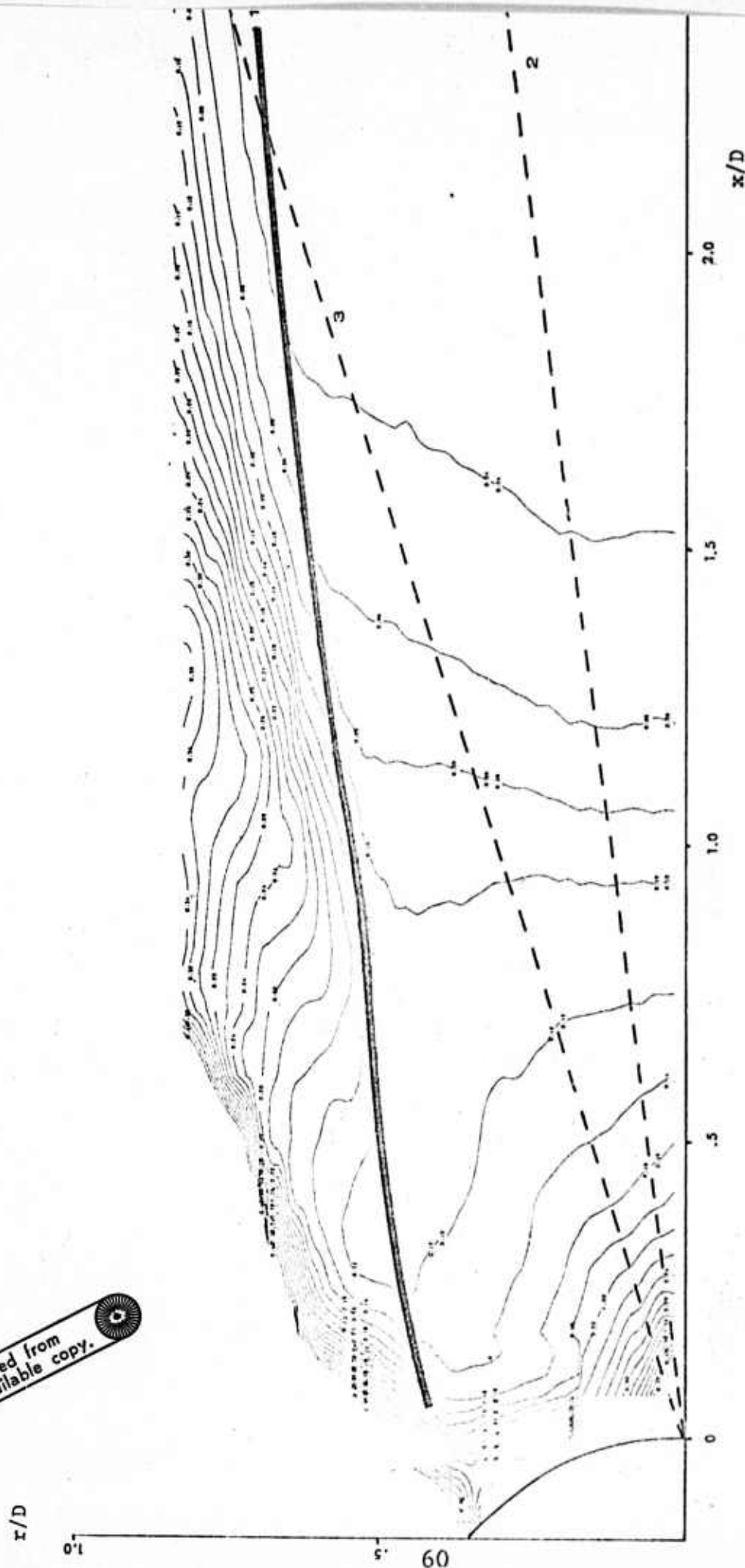


Figure 30. Specific internal energy contours in the plume inner core for the separation-free plume calculation; the contour parameter is internal energy non-dimensionalized by one tenth the free-stream stagnation internal energy; Curve 1 denotes the inner shock locus; dashed lines 2 and 3 denote inner core streamlines.

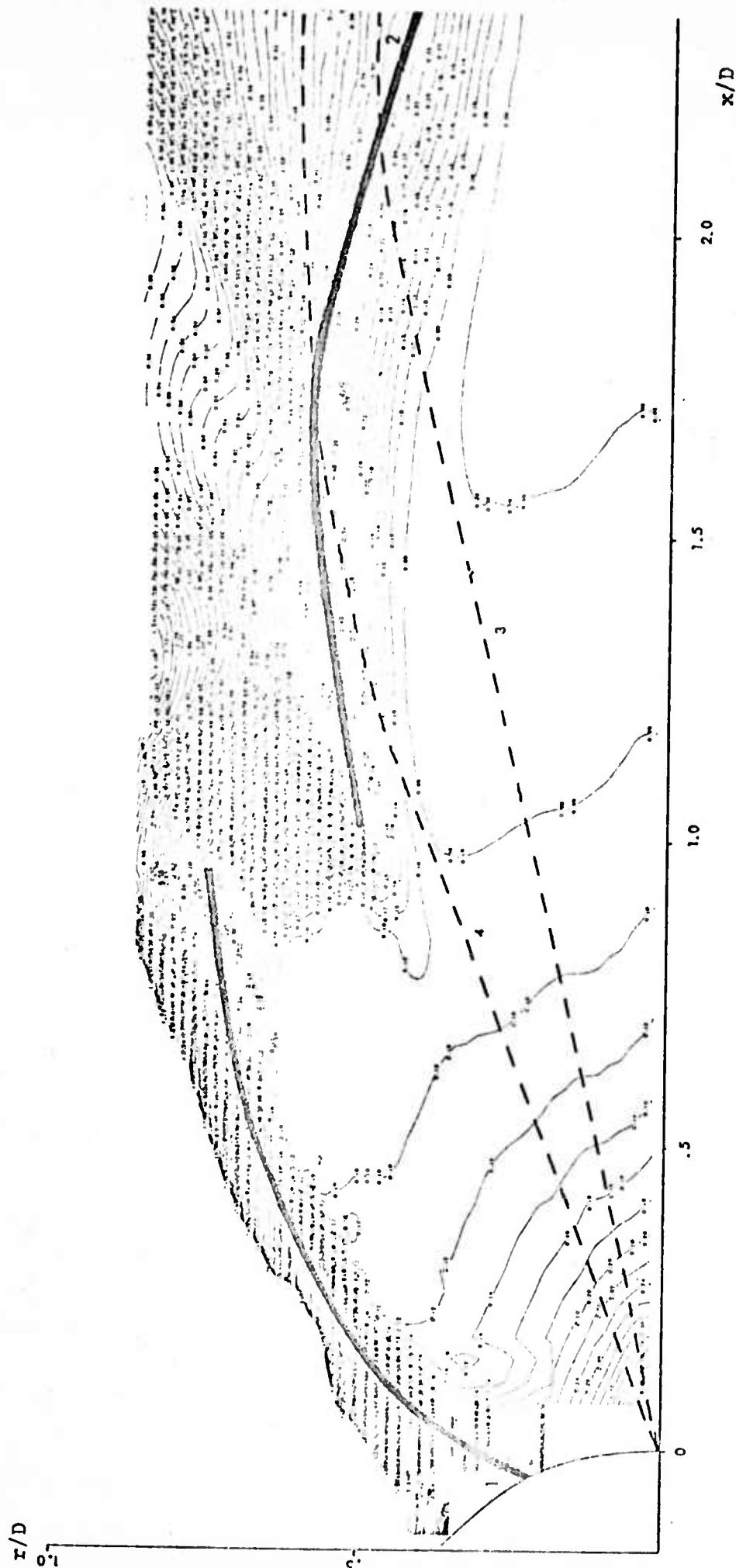


Figure 31. Specific internal energy contours in the plume inner core for the separation plume calculation; the contour parameter is internal energy non-dimensionalized by one tenth the free-stream stagnation internal energy; Curve 1 denotes the plume separation shock; Curve 2 denotes the plume inner shock; the dashed lines 3 and 4 denote inner core streamlines.

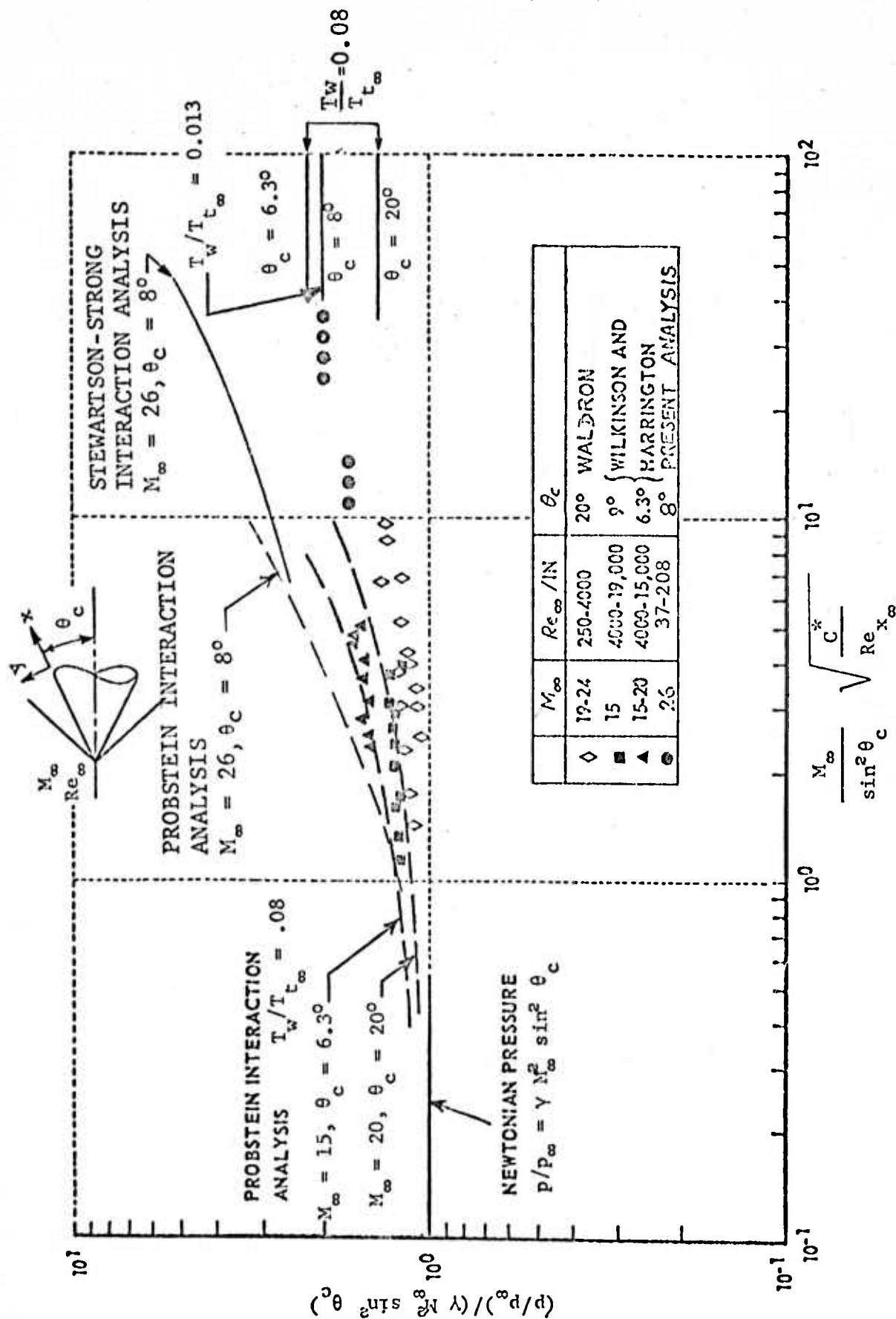


Figure 32. Correlation of cone surface pressure measurements with theoretical predictions and the numerical results of the AFTON 2A calculations.

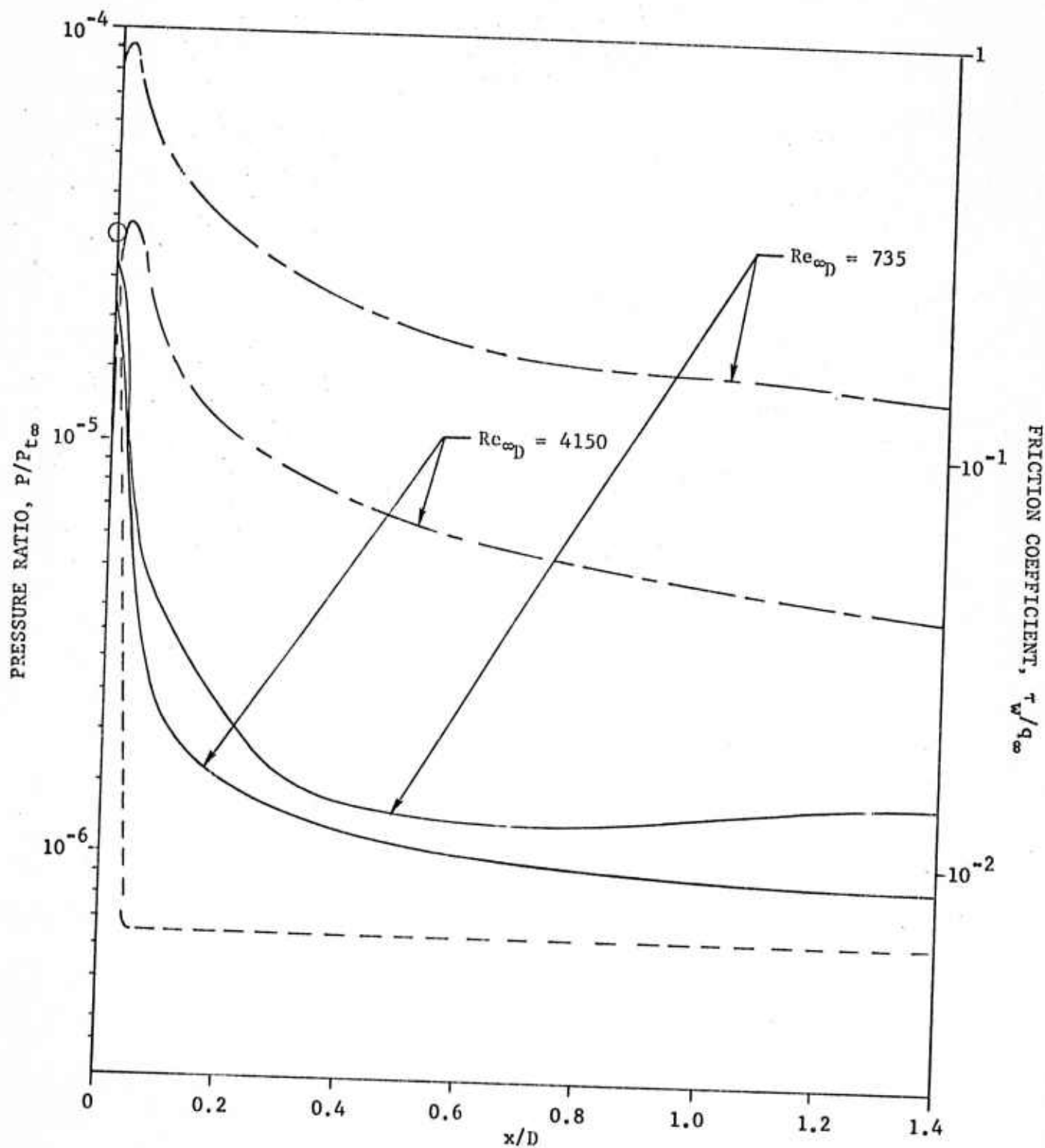


Figure 33. Pressure and shear stress distributions along the surface of the re-entry body; solid lines indicate surface pressure distributions; dashed line indicates initial surface pressure distribution (derived from Newtonian Theory); --- lines indicate surface shear stress distributions; \circ symbol denotes inviscid stagnation pressure at the leading edge of the body ($Re_{\infty D} = 735$); q_∞ and $P_{t\infty}$ denote free-stream dynamic and free-stream stagnation pressures, respectively.

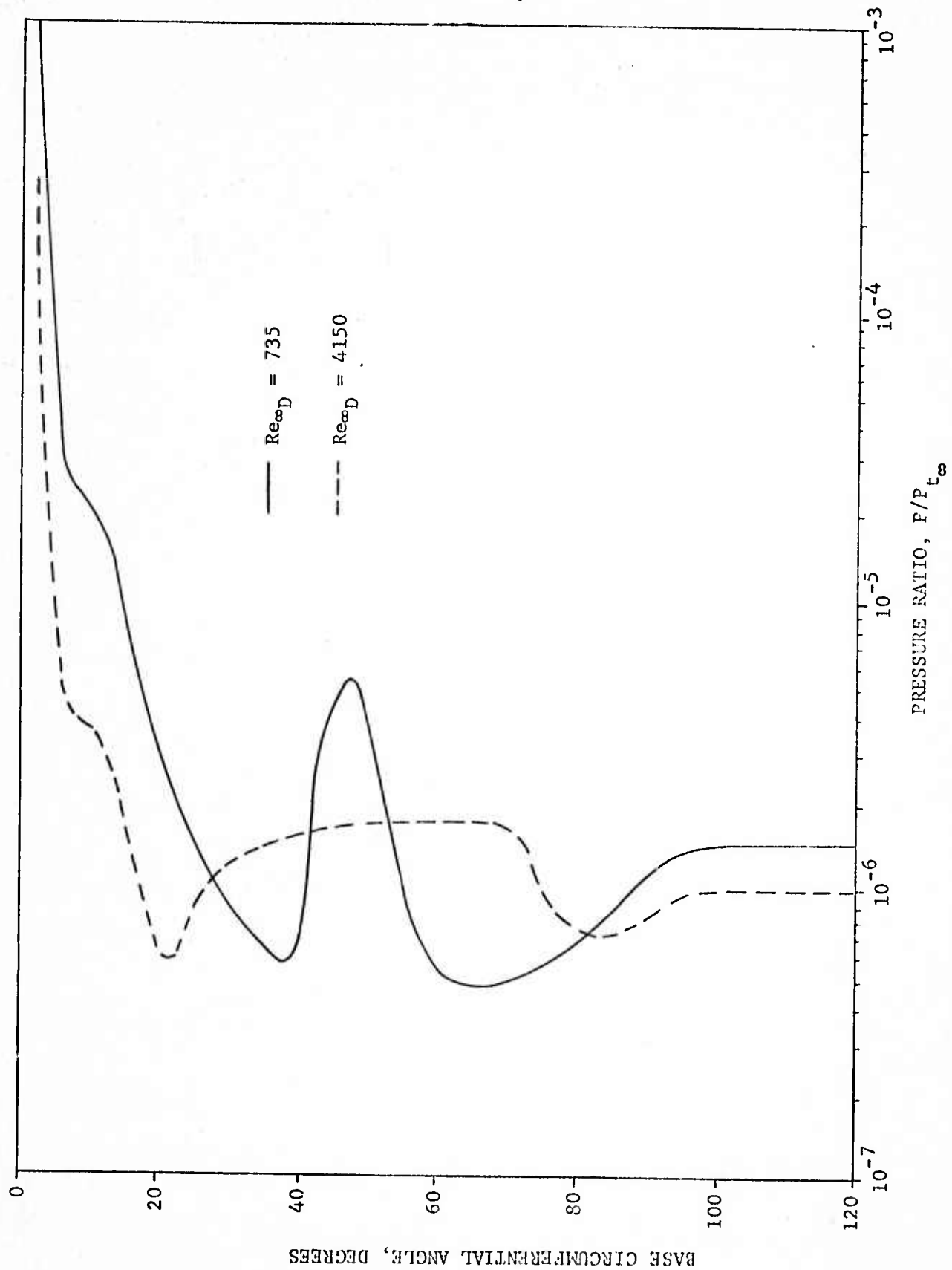


Figure 34. Steady-state base pressure distributions for re-entry body; free-stream Mach number 26.

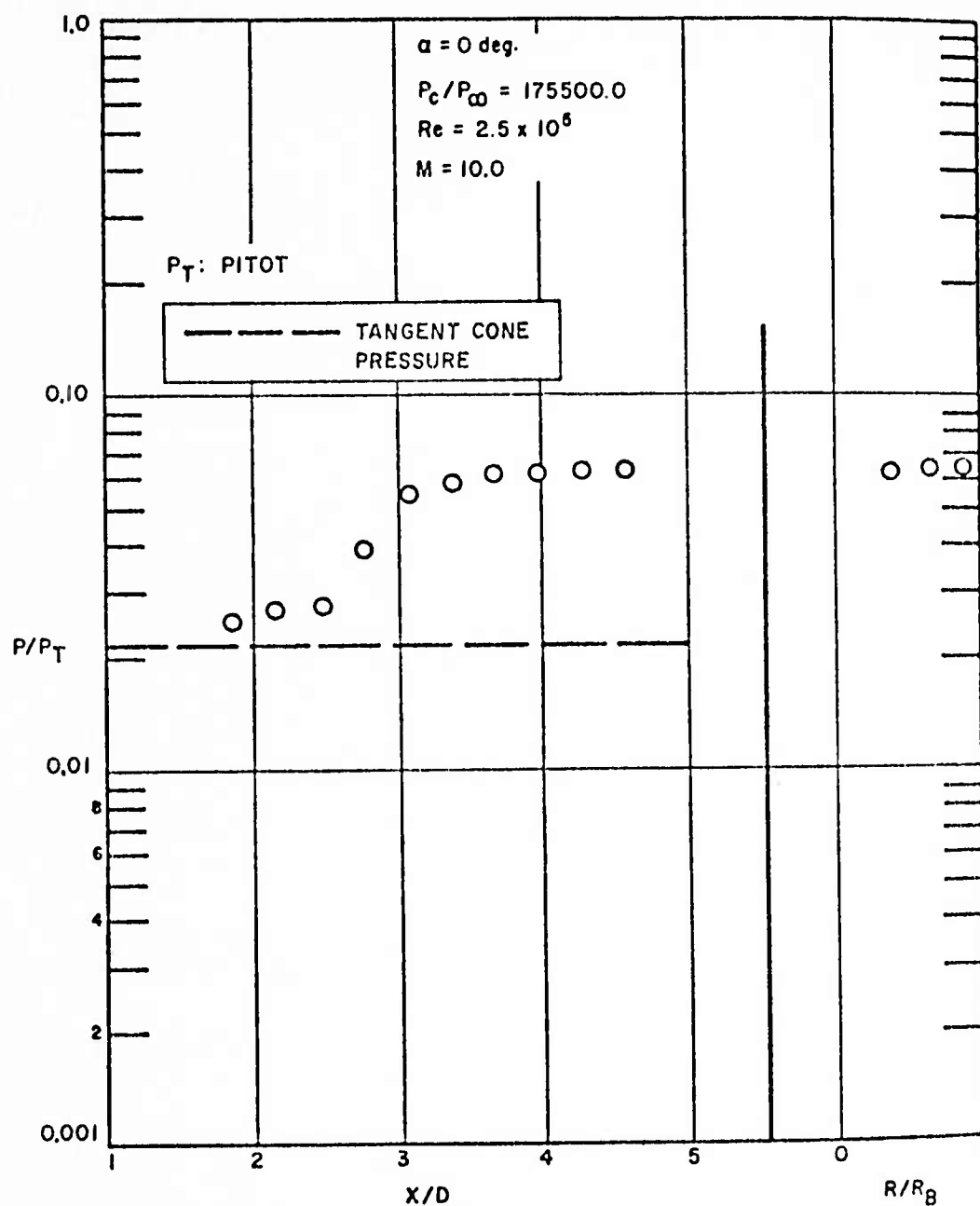


Figure 35. Plume-induced pressure distribution on a 12° flat-based cone from the measurements of Boger, Rosenbaum, and Reeves.

APPENDIX A

NUMERICAL TECHNIQUES AND CODE MODIFICATIONS

The AFTON 2A code had to be modified, and data reduction techniques developed, for the present program. Four code modifications were made, namely:

1. Provision for mass addition;
2. Inclusion of plume rarefaction effects;
3. Incorporation of an artificial viscosity function to effect shock transitions along the shock front enclosing the total region of disturbed flow;
4. Introduction of a serial calculation of heat flow and hydrodynamic motion into the computational procedure.

In addition, to aid with reduction of code output, auxiliary computer routines were written to trace streamlines and map shock waves.

A.1 Mass Addition Modification to AFTON 2A

In modifying the AFTON 2A code to simulate mass injection, it was assumed that the injected fluid and the primary fluid were identical substances, namely, viscous polytropic gases characterized by a constant polytropic exponent. Mixing of different gas components, either by convection or molecular diffusion, was not taken into account. Since conditions of no-slip flow are normally enforced at a body surface in the AFTON 2A code, the main task of code modification was that of providing for steady conditions of

discharge of jet or rocket exhaust along a portion of the base around (and including) the system axis. Code changes were made to permit the simulated emission of rocket or jet exhaust from any desired portion of the body's base, under arbitrary exit conditions; accordingly exhaust parameters of density, specific internal energy, and velocity were added to the input required to define individual problems for AFTON 2A. For the problems solved in the present program, material in a single constant flow state was injected into the flow field in a direction parallel to the system's axis.

A.2 Inclusion of Plume Rarefaction Effects in AFTON 2A

A region of highly rarefied flow is found near the axis of symmetry in the plume's inviscid core, at all free-stream conditions of interest in upper-altitude flight (source flow). The gas density approaches zero in the rarefaction region, and according to kinetic theory²⁸ its temperature, which would otherwise also approach zero, reaches a lower bound or "freezing temperature". On the basis of kinetic theory and with some hypersonic approximations, the source flow problem was reduced to a relaxation process with two translational temperatures, namely, a temperature T_{11} along streamlines, and a temperature T_1 transverse to the streamlines. Near the nozzle exit where the frequency of molecular collisions is high, $T_1 \approx T_{11}$; as collisions between gas molecules become less frequent, $T_1 \rightarrow 0$, while T_{11} remains frozen at its terminal value. For instance, for a spherical source flow, the ratio of freezing temperature T_{11} to sonic orifice temperature T^* is a function of the Knudsen number, K_{nD}^* , at the orifice, i.e.,

$$K_{n_D}^* = \lambda^*/D \quad (A1)$$

where λ^* is the mean free path at the sonic orifice and D is the orifice diameter. For the orifice gas flow state, which was identical in both calculations, the Knudsen number was $4.35 \cdot 10^{-6}$ and the freezing temperature about 70°R — a value that does not vary much with the molecular model assumed.

To impose a lower temperature bound on the order of 70°R is not only realistic for the gas, but also is useful in integrating the equations of motion numerically, since it helps prevent gas expansion to zero density. At the same time, both total mass and total thermal energy are low in the rarefaction region, and imposition of a lower temperature bound therefore has little quantitative effect on flow-field properties near the Mach disc.

The AFTON 2A computer code was modified to include a lower temperature bound, T_L , in regions of high rarefaction. For local temperatures less than or equal to T_L , the temperature (or corresponding specific internal energy) was equated to T_L . With the temperature so specified, the continuum continuity and momentum equations were solved in the usual manner for the remaining dependent variables of density and velocity.^{16,19}

A.3 Artificial Viscosity

An artificial viscosity¹⁵ proportional to the square of the velocity divergence¹² was introduced

to effect certain shock transitions. Application of the artificial viscosity was restricted to the bounding shock front that enclosed the entire disturbed region of flow; the cone shock defined the forward portion of the bounding front, with the plume shock contributing the rest. In order to minimize the possibility of introducing nonphysical effects into the flow, no artificial viscous stresses were employed in the body interaction region.

Location of the bounding shock was determined at the start of each calculational cycle by first using the artificial viscosity, designated "Q", in an indirect manner. Values of Q were calculated throughout the portion of the mesh above and including the interaction region. The Q-field was then examined along potential-like coordinate lines of the finite difference mesh (see Appendix B and Section 3.2 for a description of the AFTON 2A finite difference mesh) starting from the lateral boundary of the system and moving toward the system's axis. The first relative extremum in Q encountered on such a path defined the boundary shock front around the disturbed region of flow. However, the artificial viscosity was added to the diagonal elements of the stress tensor only in a thin band of zones clustered about the shock contours (Sections 3.2 and 4.2).

Some numerical experimentation was carried out in which the artificial viscosity was introduced into the interaction region. Details are presented in Sections 3.2 and 4.2.

A.4 Serial Calculation of Heat Conduction and Continuum Motion

To reduce computing time, the calculations of heat conduction and hydrodynamic motion were accomplished in series. Thus, advantage was taken of the fact that the time-step for the calculation was heat-diffusion-limited, and only the specific internal energy had to be updated at every time-step; other fluid properties were updated only as often as required for stable calculation in the absence of heat conduction. To compute heat flow and fluid flow sequentially two kinds of timestep were used. For hydrodynamic cycles (a "cycle" being a timestep of calculation) the time was incremented in steps, termed "macrosteps", that were small enough for the stable calculation of momentum diffusion; similarly, still smaller steps, termed "microsteps", were employed to compute thermal diffusion stably. Internal energy was updated in microstep time increments while all other hydrodynamic variables were advanced in time by macrosteps. Microsteps were so determined that each macrostep in time would always be spanned exactly by a set of consecutive microsteps. Thus the specific internal energy was updated due to heat conduction through all the microsteps that covered a given macrostep. A hydrodynamic calculation (excluding heat conduction) was then performed whereby the density, specific internal energy, and velocity were updated by the usual difference equations of motion through a macrostep.

By numerical experimentation it was established that hydrodynamic motion could be calculated as infrequently as every sixth microstep for a Reynolds number of 735, and at every other microstep at Reynolds number 4150; details are

presented in Appendix E. To test the accuracy of the procedure a portion of the lower-Reynolds-number calculation was repeated with the hydrodynamic operations performed at every timestep. The results of the test calculation agreed to four significant figures with those of the serial calculation.

A.5 Streamline Tracing and Shock-Wave Mapping

Streamlines in the AFTON-computed flow fields were determined by numerical integration of the equation

$$\frac{dr}{dx} = \frac{v}{u} \quad (A2)$$

where u and v are the velocity components in and normal to the free-stream direction, respectively. Many streamlines were traced in both the airstream and plume gases. Coalescence of plume and air streamlines defined the dividing streamline.

The positions of the various shock waves present in the computed flow fields were located by indirect use of the artificial viscosity function, Q , in a manner similar to that described in Section A.3. Specifically, after steady state conditions were attained, values of Q were computed throughout the numerical flow field. Contours of maximum Q were then located manually and identified as the shock loci; by examining the artificial viscosity function along each coordinate line of the mesh (either streamline-like or potential-like, as in Figure B1) and thereby locating extrema along the line; the locus of an extremum defined a shock front.

APPENDIX B

A SCHEME FOR CALCULATING POSITIONS OF POINTS IN FINITE DIFFERENCE MESHES

A technique was developed and used in the present study to assign to the points of a finite difference mesh positions suited to the calculation of flow past a round-based conical body. The method consists of generating two families of non-intersecting lines (streamline-like lines and potential-like lines) which merge smoothly with prescribed sets of control lines; points of intersection of the two families define the mesh. The location-specifying equations represent a mapping between integer variables (j,k) and the axial and radial (x,r) coordinates of a point; in the AFTON 2A code, an integer k is associated with each potential-like coordinate line, and an integer j is associated with each streamline-like coordinate line.

A schematic of a typical set of control lines is shown in Figure B1, together with dashed lines that represent j -lines and k -lines. Two streamline-like control lines and four potential-like control lines are used in the process of mesh construction described here. The lateral boundary of the mesh ($j = j_\ell$) and the body-surface-and-axis contour ($j = j_b$) are streamline-like control lines, while the potential-like control lines are the curves designated by the k -indices k_u , k_b , k_t and k_d ; in the present study, the k -control lines were chosen as parabolas. Coordinates of points on the various control lines were found by assigning values to one of the two coordinates in accord with a geometric progression; the value of the other coordinate followed from the known analytic expression for the shape of the control

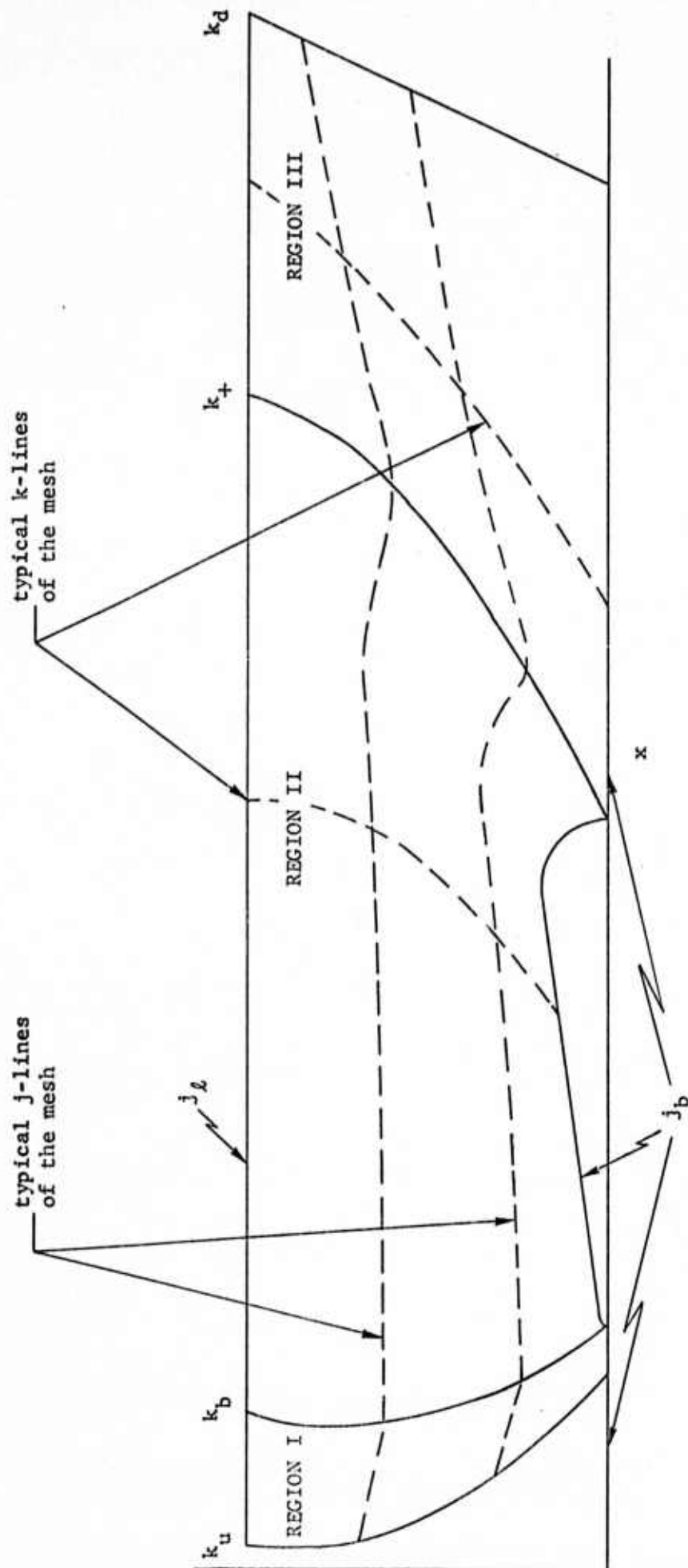


Figure B1. Schematic of the control lines for development of mesh-point coordinates for a round-based cone; the dashed lines represent coordinate lines of the mesh of the streamline-like and potential-like variety.

line. For example, along the potential-like control line $k = k_b$, the following relations were employed. For $j_b \leq j \leq j_\ell$,

$$\left. \begin{aligned} r(j, k_b) &= r(j_b, k_b) + \frac{\Delta_1 (1 - \gamma_1^{j-j_b})}{(1 - \gamma_1)} \\ x(j, k_b) &= B_1 y^2(j, k_b) + B_2 y(j, k_b) + B_3 \\ \Delta_1 &= \frac{[r(j_\ell, k_b) - r(j_b, k_b)] (1 - \gamma_1)}{(1 - \gamma_1^{j_\ell - j_b})} \end{aligned} \right\} \quad (B1)$$

where γ_1 is the rate of increase of spacing of the mesh points, Δ_1 is the minimum increment between mesh points, and B_1 , B_2 , and B_3 are known constants.

The technique was implemented by generating mesh-point coordinates in each of the three regions shown in Figure B1. A smoothing function was then used to guarantee continuous slope for the streamline-like lines at the boundaries of the three regions. For each region, the coordinates were calculated from equations of the form

$$r(j, k) = F_L^r r(j_\ell, k) + F_B^r r(j_b, k) \quad (B2)$$

and

$$x(j, k) = F_L^x x(j_\ell, k) + F_B^x x(j_b, k) \quad (B3)$$

where F_L^r , F_B^r , F_L^x , and F_B^x are weighting functions. The weighting functions for the three regions are presented below.

REGION I

The radial coordinate weighting functions are defined as follows:

$$F_L^r = F_{1L}^r \left[\frac{x(j_\ell, k_b) - x(j_\ell, k)}{x(j_\ell, k_b) - x(j_\ell, k_u)} \right] + F_{2L}^r \left[\frac{x(j_\ell, k) - x(j_\ell, k_u)}{x(j_\ell, k_b) - x(j_\ell, k_u)} \right]$$

where

$$F_{1L}^r = \left[\frac{r(j, k_u) - r(j_b, k_u)}{r(j_\ell, k_u) - r(j_b, k_u)} \right]$$

and

$$F_{2L}^r = \left[\frac{r(j, k_b) - r(j_b, k_b)}{r(j_\ell, k_b) - r(j_b, k_b)} \right]$$

$$F_B^r = F_{1B}^r \left[\frac{x(j_b, k_b) - x(j_b, k)}{x(j_b, k_b) - x(j_b, k_u)} \right] + F_{2B}^r \left[\frac{x(j_b, k) - x(j_b, k_u)}{x(j_b, k_b) - x(j_b, k_u)} \right]$$

where

$$F_{1B}^r = \left[\frac{r(j_\ell, k_u) - r(j, k_u)}{r(j_\ell, k_u) - r(j_b, k_u)} \right]$$

and

$$F_{2B}^r = \left[\frac{r(j_\ell, k_b) - r(j, k_b)}{r(j_\ell, k_b) - r(j_b, k_b)} \right]$$

Weighting functions for the axial coordinate are:

$$F_L^x = F_{1L}^x \left[\frac{x(j_\ell, k_b) - x(j_\ell, k)}{x(j_\ell, k_b) - x(j_\ell, k_u)} \right] + F_{2L}^x \left[\frac{x(j_\ell, k) - x(j_\ell, k_u)}{x(j_\ell, k_b) - x(j_\ell, k_u)} \right]$$

where

$$F_{1L}^x = \left[\frac{x(j_\ell, k_u) - x(j, k_u)}{x(j_\ell, k_u) - x(j_b, k_u)} \right]$$

and

$$F_{2L}^x = \left[\frac{x(j_\ell, k_b) - x(j, k_b)}{x(j_\ell, k_b) - x(j_b, k_b)} \right]$$

$$F_B^x = F_{1B}^x \left[\frac{x(j_b, k_b) - x(j_b, k)}{x(j_b, k_b) - x(j_b, k_u)} \right] + F_{2B}^x \left[\frac{x(j_b, k) - x(j_b, k_u)}{x(j_b, k_b) - x(j_b, k_u)} \right]$$

where

$$F_{1B}^x = \left[\frac{x(j_\ell, k_u) - x(j, k_u)}{x(j_\ell, k_u) - x(j_b, k_u)} \right]$$

and

$$F_{2B}^x = \left[\frac{x(j_\ell, k_b) - x(j, k_b)}{x(j_\ell, k_b) - x(j_b, k_b)} \right]$$

REGION II

For the radial coordinate, the weighting functions are:

$$F_L^r = F_{1L}^r \left[\frac{x(j_\ell, k_t) - x(j_\ell, k)}{x(j_\ell, k_t) - x(j_\ell, k_b)} \right] + F_{2L}^r \left[\frac{x(j_\ell, k) - x(j_\ell, k_b)}{x(j_\ell, k_t) - x(j_\ell, k_b)} \right]$$

where

$$F_{1L}^r = \left[\frac{r(j, k_b) - r(j_b, k_b)}{r(j_\ell, k_b) - r(j_b, k_b)} \right]$$

and

$$F_{2L}^r = \left[\frac{r(j, k_t) - r(j_b, k_t)}{r(j_\ell, k_t) - r(j_b, k_t)} \right]$$

$$F_B^r = F_{1B}^r \left[\frac{x(j_b, k_t) - x(j_b, k)}{x(j_b, k_t) - x(j_b, k_b)} \right] + F_{2B}^r \left[\frac{x(j_b, k) - x(j_b, k_b)}{x(j_b, k_t) - x(j_b, k_b)} \right]$$

where

$$F_{1B}^r = \left[\frac{r(j_\ell, k_b) - r(j, k_b)}{r(j_\ell, k_b) - r(j_b, k_b)} \right]$$

and

$$F_{2B}^r = \left[\frac{r(j_\ell, k_t) - r(j, k_t)}{r(j_\ell, k_t) - r(j_b, k_t)} \right]$$

The weighting functions for use in calculation of the x-coordinate in Region II are defined as follows:

$$F_L^x = F_{1L}^x \left[\frac{x(j_\ell, k_t) - x(j_\ell, k)}{x(j_\ell, k_t) - x(j_\ell, k_b)} \right] + F_{2L}^x \left[\frac{x(j_\ell, k) - x(j_\ell, k_b)}{x(j_\ell, k_t) - x(j_\ell, k_b)} \right]$$

where

$$F_{1L}^x = \left[\frac{x(j, k_b) - x(j_b, k_b)}{x(j_\ell, k_b) - x(j_b, k_b)} \right]$$

and

$$F_{2L}^x = \left[\frac{x(j, k_t) - x(j_b, k_t)}{x(j_\ell, k_t) - x(j_b, k_t)} \right]$$

$$F_B^x = F_{1B}^x \left[\frac{x(j_b, k_t) - x(j_b, k)}{x(j_b, k_t) - x(j_b, k_b)} \right] + F_{2B}^x \left[\frac{x(j_b, k) - x(j_b, k_b)}{x(j_b, k_t) - x(j_b, k_b)} \right]$$

where

$$F_{1B}^x = \left[\frac{x(j_\ell, k_b) - x(j, k_b)}{x(j_\ell, k_b) - x(j_b, k_b)} \right]$$

and

$$F_{2B}^x = \left[\frac{x(j_\ell, k_t) - x(j, k_t)}{x(j_\ell, k_t) - x(j_b, k_t)} \right]$$

REGION III

The weighting functions for the r-coordinate are:

$$F_L^r = F_{1L}^r \left[\frac{x(j_{\ell}, k_d) - x(j_{\ell}, k)}{x(j_{\ell}, k_d) - x(j_{\ell}, k_t)} \right] + F_{2L}^r \left[\frac{x(j_{\ell}, k) - x(j_{\ell}, k_t)}{x(j_{\ell}, k_d) - x(j_{\ell}, k_t)} \right]$$

where

$$F_{1L}^r = \left[\frac{r(j, k_t) - r(j_b, k_t)}{r(j_{\ell}, k_t) - r(j_b, k_t)} \right]$$

and

$$F_{2L}^r = \left[\frac{r(j, k_d) - r(j_{\ell}, k_d)}{r(j_{\ell}, k_d) - r(j_{\ell}, k_t)} \right]$$

$$F_B^r = F_{1B}^r \left[\frac{x(j_b, k_d) - x(j_b, k)}{x(j_b, k_d) - x(j_b, k_t)} \right] + F_{2B}^r \left[\frac{x(j_b, k) - x(j_b, k_t)}{x(j_b, k_d) - x(j_b, k_t)} \right]$$

where

$$F_{1B}^r = \left[\frac{r(j_{\ell}, k_t) - r(j, k_t)}{r(j_{\ell}, k_t) - r(j_b, k_t)} \right]$$

and

$$F_{2B}^r = \left[\frac{r(j_{\ell}, k_d) - r(j, k_d)}{r(j_{\ell}, k_d) - r(j_{\ell}, k_t)} \right]$$

The weighting functions for the x-coordinate are defined by the following relations:

$$F_L^x = F_{1L}^x \left[\frac{x(j_{\ell}, k_d) - x(j_{\ell}, k)}{x(j_{\ell}, k_d) - x(j_{\ell}, k_t)} \right] + F_{2L}^x \left[\frac{x(j_{\ell}, k) - x(j_{\ell}, k_t)}{x(j_{\ell}, k_d) - x(j_{\ell}, k_t)} \right]$$

where

$$F_{1L}^x = \left[\frac{x(j, k_t) - x(j_b, k_t)}{x(j_{\ell}, k_t) - x(j_b, k_t)} \right]$$

and

$$F_{1L}^x = \left[\frac{x(j, k_d) - x(j_b, k_d)}{x(j_\ell, k_d) - x(j_b, k_d)} \right]$$

$$F_B^x = F_{1B}^x \left[\frac{x(j_b, k_d) - x(j_b, k)}{x(j_b, k_d) - x(j_b, k_t)} \right] + F_{2B}^x \left[\frac{x(j_b, k) - x(j_b, k_t)}{x(j_b, k_d) - x(j_b, k_t)} \right]$$

where

$$F_{1B}^x = \left[\frac{x(j_\ell, k_t) - x(j, k_t)}{x(j_\ell, k_t) - x(j_b, k_t)} \right]$$

and

$$F_{2B}^x = \left[\frac{x(j_\ell, k_d) - x(j, k_d)}{x(j_\ell, k_d) - x(j_b, k_d)} \right]$$

APPENDIX C

PREDICTION OF SHOCK STRUCTURE IN THE INTERACTION REGION BY THE METHOD OF CHARACTERISTICS

By means of shadowgraphs, pressure measurements, and the method of characteristics, Boger, Rosenbaum, and Reeves⁶ described the complicated flow phenomena associated with the interaction between the plume and external flow (leaving the cone surface) in the base region of a flat-based cone with a vertex angle of 12° . The body was immersed in a Mach 10 air-stream at Reynolds number $1.29 \cdot 10^6$ with a chamber-to-ambient pressure ratio (p_c/p_∞) of $2.2 \cdot 10^4$. These conditions produced a plume which did not induce separation on the cone forebody; the base flow field was therefore amenable to analysis by classical methods. However, at the point where the inner shear layer edge of the external flow impinged on the plume gases, the multiple-shock pattern produced is identical to that of plume-induced cone-forebody separation (see Figure 21). An interpretation of the shock structure for the non-separated case is therefore directly applicable to the separated case.

Figure C1 shows the flow just behind the cone base. The plume boundary expands nearly 90 degrees at the nozzle lip, but gradually bends away from the base, with a plume separation shock forcing the fluid to move in a direction parallel to the boundary. The boundary and shock are obtained from a method-of-characteristics calculation with the experimental values of chamber pressure and base pressure as input quantities. At the point where the plume flow and external flow meet, the plume separation shock turns very rapidly and a second shock (designated the plume shock) is formed in the

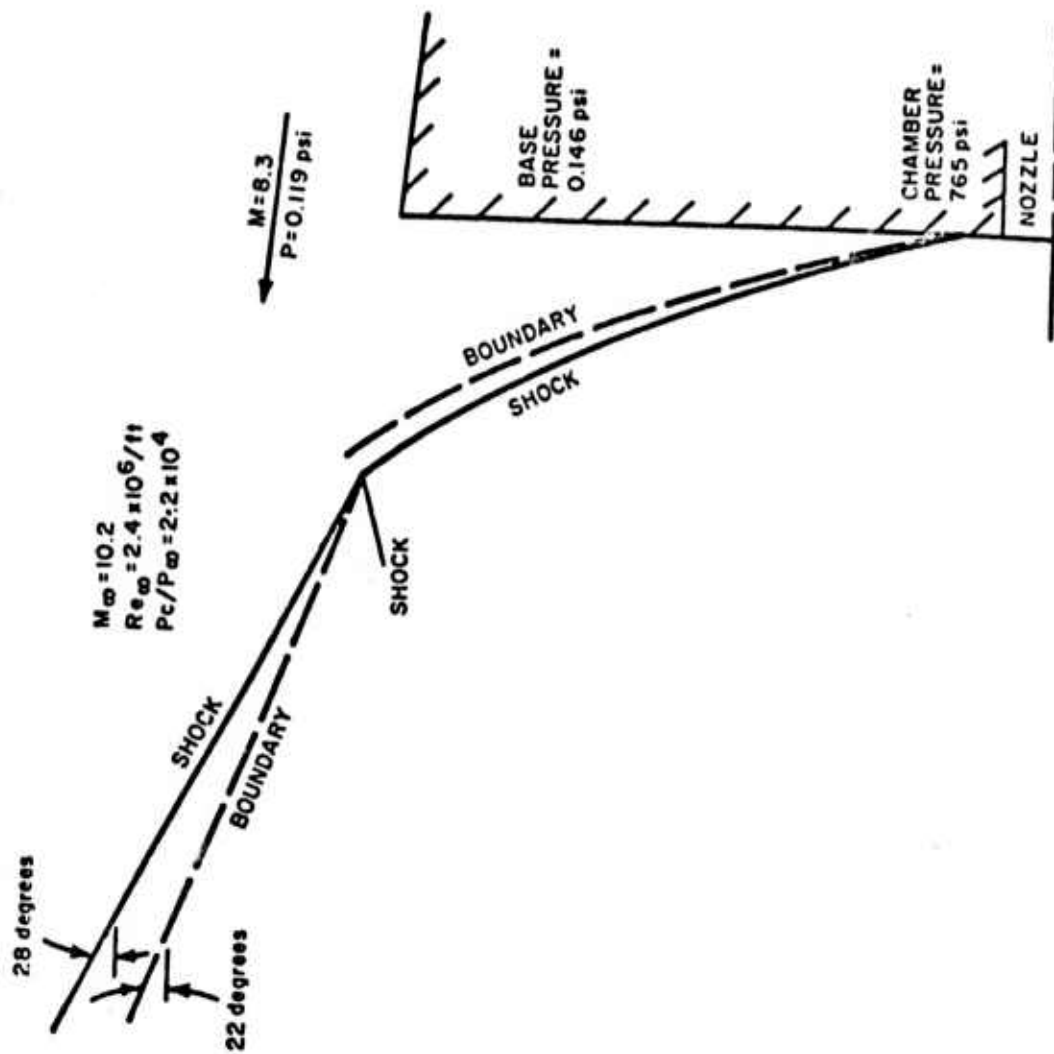
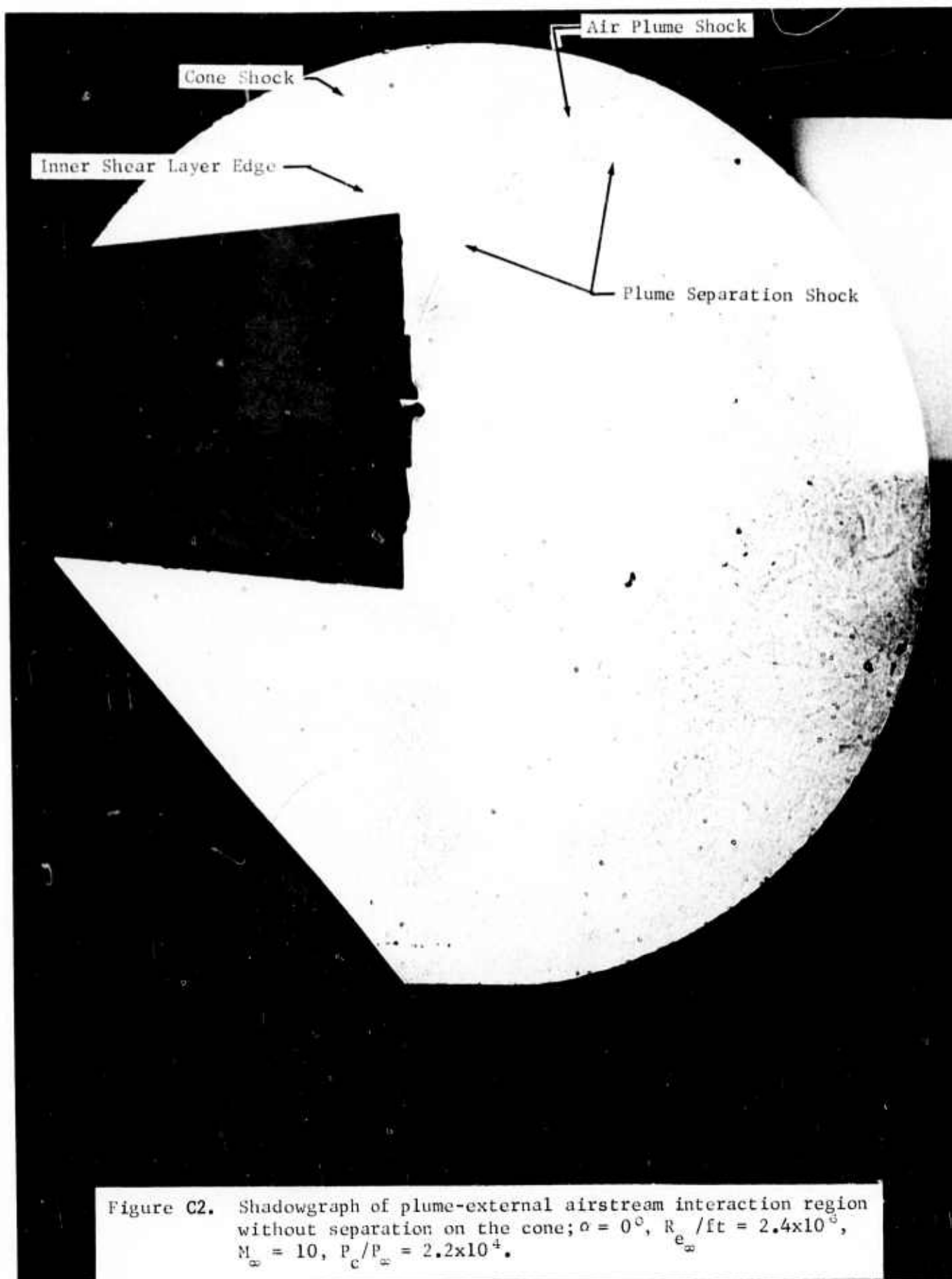


Figure C1. Interaction between the plume and the external flow in the base region about a 12° flat-based cone.

external stream. The shock and boundary locations of Figure C1 are obtained by calculating the deflection angles for the plume and external flows in order that they share a common pressure boundary. Calculated directions of the shocks and plume boundary agree with the shadowgraph of the flow field shown in Figure C2. Features of the field visible on the shadowgraph include the cone shock, plume shock, plume separation shock, and the boundary of the shear layer leaving the end of the cone.



APPENDIX D

EFFECTS OF NOSE BLUNTNESS ON THE CONE FLOW FIELD

Since the re-entry body of Figure 1 is rounded (radius = 1.2 inches) and not pointed at its upstream tip, it is appropriate to consider the effects of nose bluntness on the computed flow fields; such effects are superimposed on the effects of viscous-inviscid interaction.

The relative importance of viscous-inviscid interaction and nose bluntness depends on the leading-edge Reynolds number, i.e.,

$$Re_{\infty d_n} = \frac{\rho_{\infty} U_{\infty} d_n}{\mu_{\infty}} \quad (D1)$$

where d_n is the nose diameter, U_{∞} the free-stream velocity, ρ_{∞} the free-stream density and μ_{∞} the free-stream viscosity. Experimentally, it is known for cones that when $Re_{\infty d_n}$ is less than 100, leading-edge-bluntness effects may be considered negligible compared to the effects of interaction between the viscous layer and the external inviscid flow.²⁹ For the separation-free plume problem, the Reynolds number, based on the nose diameter, is $Re_{\infty d_n} = 89$; for the separation plume problem, the Reynolds number is $Re_{\infty d_n} = 500$. Thus, bluntness effects should be small when compared to the effects of viscous-inviscid interaction for the separation-free plume problem, but should become more significant for the separation-plume problem.

The possibility of important nose-bluntness effects in the present study became very remote when it was shown for

both the flows calculated that rounding the nose of the cone had little influence on the pressure distribution halfway down the cone forebody. To decide the issue, use was made of a correlation of the effect of nose bluntness on the pressure distribution about a cone; the correlation was derived by Griffith and Lewis²⁵ from pressure measurements taken about various blunt-nosed cones at different Reynolds numbers and in the Mach number range 10 to 20. An approximate fairing through the Griffith-Lewis data is presented in Figure D1. The abscissa of Figure D1 is used to define values of the parameter

$$\chi_c = (x/d_n) [\theta_c^2 / (\epsilon k)^{\frac{1}{2}}] \quad (D2)$$

where x is axial position measured from the cone nose, θ_c is the cone-half angle, ϵ is the compression ($\epsilon \equiv \frac{\gamma-1}{\gamma+1}$), and k the nose-drag coefficient, is equal to .964 for a spherically blunt cone. The ratio of the local pressure coefficient to the Newtonian pressure coefficient is specified along the ordinate of the figure. It can be seen that in the Mach number range 10 to 20, the pressure change (relative to the slender body limit) arising from nose bluntness varies with axial position, cone half-angle, cone diameter, and compression. For the two problems solved in this numerical study the parameter χ_c had the value 1.47 halfway down the cone, where it is therefore evident from the figure that in the cases of interest here the pressure is nearly asymptotic to its slender-body value.

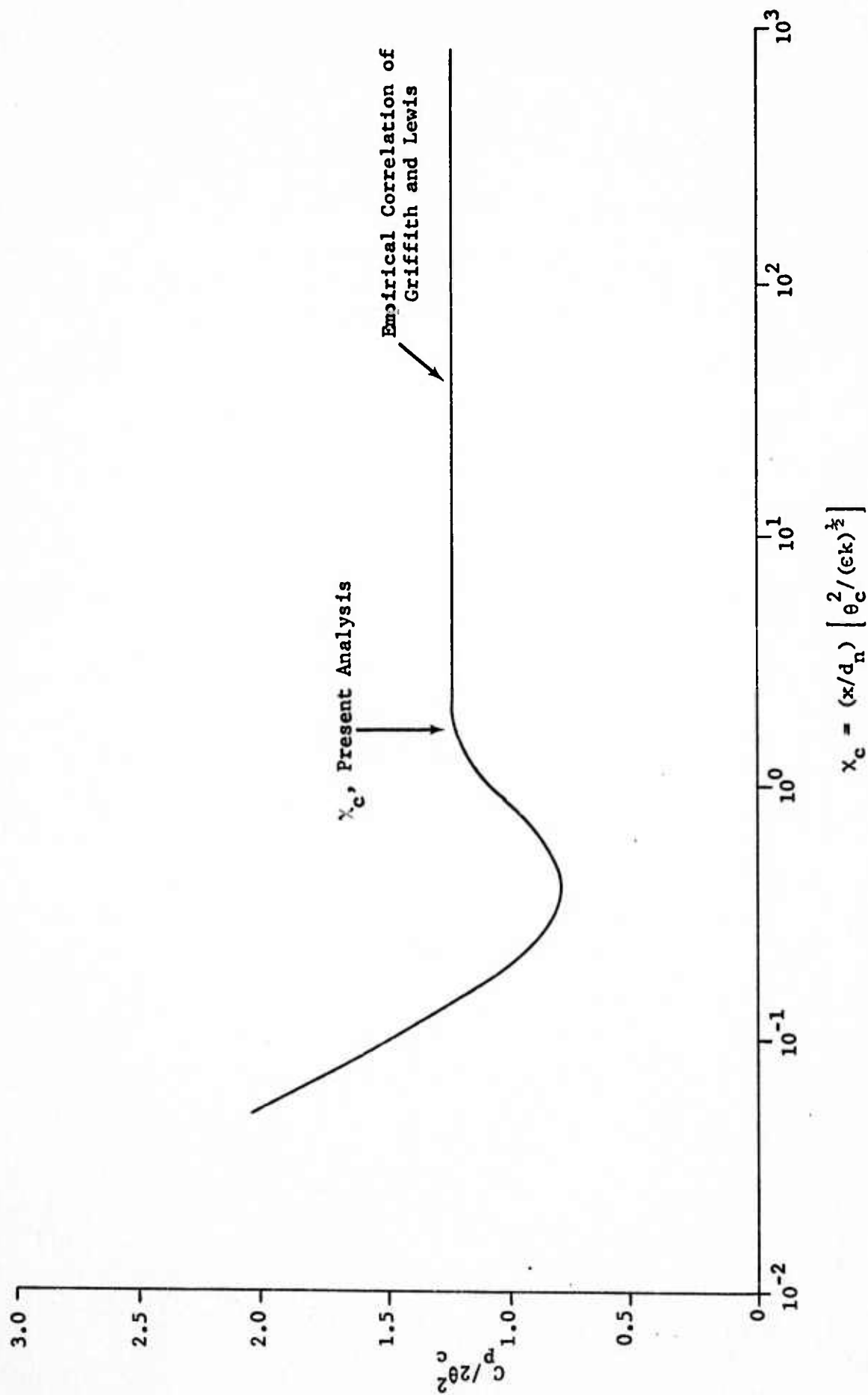


Figure D1. Effect of nose bluntness on the pressure distribution about a cone.

APPENDIX E

STABILITY CRITERIA FOR AFTON 2A

For the AFTON codes, as for almost all practical tools for time-marching integration of the equations of continuum motion, considerations of numerical stability dictate that the timestep not exceed a finite flow- and mesh-dependent upper bound. In the plume calculations reported here, diffusive processes - thermal and momentum diffusion in the heat conduction and hydrodynamic phases of computation - always limited the timestep. Sequential calculation of heat conduction and hydrodynamic motion offered an attractive path to improved computational efficiency because the timestep limits Δt_t and Δt_v associated with thermal and viscous diffusion, respectively, differed considerably; Δt_t and Δt_v are defined by the formulas

$$\Delta t_t = \frac{1}{2} \Delta^2 / \alpha_t \quad (E1)$$

$$\Delta t_v = \frac{1}{2} \Delta^2 / \nu \quad (E2)$$

where Δ is the zone width of the least stable zone of the mesh, α_t is thermal diffusivity and ν is kinematic viscosity.

It was found³⁰ that for a Reynolds number of 735 the calculation proceeded stably with timesteps of $.8 \Delta t_t$ and $.7 \Delta t_v$, respectively, for heat conduction and viscous momentum diffusion. However, the numerical flow field then oscillated spatially and in time with large but bounded amplitude; a further increase by a factor of two in either timestep resulted in unstable oscillation of the field. Thus, the stability properties of the AFTON 2A code do not differ significantly

from those predicted by simple stability theory.

The amplitudes of the nonphysical oscillations produced with timesteps of $.8 \Delta t_t$ and $.7 \Delta t_v$ had to be greatly reduced to obtain numerical solutions of acceptable accuracy. To that end it was established by numerical trial-and-error that satisfactory solutions were produced using a heat-conduction timestep equal to $.25 \Delta t_t$ and a timestep of $.7 \Delta t_v$ for viscous momentum diffusion, and those timesteps were actually used to carry out the calculation for a Reynolds number of 735. For a Reynolds number of 4150, thermal and viscous timesteps of $\frac{1}{4} \Delta t_t$ and $\frac{1}{4} \Delta t_v$ were used, after again establishing by numerical experimentation that acceptable numerical solutions would then be obtained.

REFERENCES

1. Jarvinen, P.O., and Hill, J.A.F., "Universal Model for Underexpanded Rocket Plumes in Hypersonic Flows," presented at the 12th JANNAF Liquid Propulsion Meeting, Las Vegas (November 1970).
2. Jarvinen, P.O., and Dyner, H.B., "Rocket Exhaust Plume Dimensions," J. Spacecraft, Volume 6, No. 11, p. 1309 (1969).
3. Boynton, F.P., and Thomson, A., "Numerical Computations of Steady, Supersonic Two-Dimensional Gas Flow in Natural Coordinates," Journal of Computational Physics, 3, p. 379 (1969).
4. Sherman, F.S., "A Source Model of Viscous Effects in Hypersonic Axisymmetric Free Jets," Arch. Mech. Stosowanej, Vol. 2, No. 16, p. 472 (1964).
5. Roberts, L., "The Action of a Hypersonic Jet on a Dust Layer," IAS Paper No. 63-50 (1963).
6. Boger, R.C., Rosenbaum, H., and Reeves, B.L., "Flowfield Interactions Induced by Underexpanded Exhaust Plumes," AIAA Journal, 10, p. 300 (1972).
7. Trulio, J.G., Niles, W.J., Carr, W.E., and Rentfrow, R.L., "Calculations of Two-Dimensional Turbulent Flow Fields," NASA CR-430 (1966).
8. Trulio, J.G., and Walitt, L., "Numerical Calculation of Viscous Compressible Fluid Flow Around an Oscillating Rigid Cylinder," NASA CR-1467 (1969).
9. Trulio, J.G., and Walitt, L., "Numerical Calculations of Separated Flows," Symposium on Viscous Interaction Phenomena in Supersonic and Hypersonic Flow, University of Dayton Press (1969).
10. Walitt, L., "Numerical Studies of Supersonic Near Wakes," Ph.D. Dissertation, University of California at Los Angeles (1969); also Report No. 69-26, School of Engineering and Applied Science, UCLA (1969).

REFERENCES (continued)

11. Trulio, J.G., and Walitt, L., "Numerical Calculations of Viscous Compressible Fluid Flow Around a Stationary Cylinder," NASA CR-1467 (1969).
12. Walitt, L., Trulio, J.G., and Liu, C.Y., "Numerical Calculations of Flow About a 20° Flat-Based Wedge Under Hypersonic Conditions," Applied Theory Report No. ATR-22-72 (1972).
13. Srinivasa, D., Trulio, J.G., and Liu, C.Y., "A Time-Dependent Method for Problems with Axial Symmetry and Its Application to Hypersonic Near Wake," Applied Theory Report to be published (1973).
14. Walitt, L., Trulio, J.G., and King, L.S., "A Numerical Method for Computing Three-Dimensional Viscous Supersonic Flow Fields About Slender Bodies," Proceedings of the Symposium on Analytical Methods in Aircraft Aerodynamics, Ames Research Center, NASA SP-228 (1969); also NASA CR-1963 (1971).
15. von Neumann, S., and Richtmyer, R., "A Method for the Numerical Calculation of Hydrodynamic Shocks," J. Applied Physics, 21, p. 232 (1950).
16. Trulio, J.G., "Theory and Structure of the AFTON Codes," AFWL-TR-60-19 (1960).
17. Trulio, J.G., and Trigger, K.R., "Numerical Solution of the One-Dimensional Lagrangian Hydrodynamic Equations," UCRL-6267 (1961).
18. Trulio, J.G., Carr, W.E., and Mullen, J.B., "PUFF Rezone Development," AFWL-TR-69-50 (1969).
19. Trulio, J.G., "Notes on the Eulerian AFTON Equations for Fluid Mechanics Calculations," ATR-73-33-1 (1973).
20. Batt, R.B., and Kubota, T., "Experimental Investigation of Laminar Near Wake Behind a 20° Wedge at $M = 6$," AIAA Journal, Vol. 6, No. 11, p. 2077-2083 (1968).

REFERENCES (continued)

21. Schlichting, H., Boundary Layer Theory, Fourth Edition, McGraw-Hill, p. 245 (1960).
22. Kawaguti, M., and Jain, Padam, "Numerical Study of Viscous Fluid Past a Circular Cylinder," MRC Technical Summary Report #590, University of Wisconsin (1965).
23. Waldron, H.F., "Viscous Hypersonic Flow Over Pointed Cones at Low Reynolds Numbers," AIAA Paper 66-34, AIAA 3rd Aerospace Science Meeting, New York (January 1966).
24. Wilkinson, D.B., and Harrington, S.A., "Hypersonic Force, Pressure, and Blunt Slender Cones," AEDC TDP-63-171 (1963).
25. Griffith, B.J., and Lewis, C.H., "Laminar Heat Transfer to Spherically Blunted Cones at Hypersonic Conditions," AIAA Journal, 2, p. 438 (1964).
26. Probst, R.F., "Interacting Hypersonic Laminar Boundary Layer Flow Over a Cone," Technical Report AF 279811, Brown University (1955).
27. Stewartson, K., "Viscous Hypersonic Flow Past a Slender Cone," Physics of Fluids, 2, p. 5 (1964).
28. Hamel, B.B., and Willis, D.R., "Kinetic Theory as Source Flow Expansion with Application to the Free Jet," Phys. of Fluids, Vol. 9, No. 5, p. 529 (1966).
29. Cox, R.N., and Crabtree, L.F., Elements of Hypersonic Aerodynamics, p. 195-198, Academic Press (1965).
30. Applied Theory, Inc. letter, J.G. Trulio, to R. H. Lee of Aerospace Corporation, "Stability of the AFTON Finite Difference Equations," July 1972.